

# NeuralCrop: Combining physics and machine learning for improved crop yield projections

Yunan Lin<sup>1,2\*</sup>, Sebastian Bathiany<sup>1,2</sup>, Maha Badri<sup>1,2</sup>,  
Maximilian Gelbrecht<sup>1,2</sup>, Philipp Hess<sup>1,2</sup>, Brian Groenke<sup>2</sup>,  
Jens Heinke<sup>2</sup>, Christoph Müller<sup>2</sup>, Niklas Boers<sup>1,2,3\*</sup>

<sup>1</sup>Munich Climate Center and Earth System Modelling Group,  
Department of Aerospace and Geodesy, School of Engineering and  
Design, Technical University of Munich, Munich, Germany.

<sup>2</sup>Potsdam Institute for Climate Impact Research, Potsdam, Germany.

<sup>3</sup>University of Exeter, Exeter, UK.

\*Corresponding author(s). E-mail(s): [yunan.lin@tum.de](mailto:yunan.lin@tum.de);  
[n.boers@tum.de](mailto:n.boers@tum.de);

## Abstract

Global gridded crop models (GGCMs) are crucial to project the impacts of climate change on agricultural productivity and assess associated risks for food security. Despite decades of development, state-of-the-art GGCMs retain substantial uncertainties stemming from process representations. Recently, machine learning approaches trained on observational data provide alternatives in crop yield projections. However, these models have not demonstrated improved performance over traditional GGCMs and are not suitable for projecting crop yields under a changing climate due to their poor out-of-distribution generalization. Here we introduce NeuralCrop, a differentiable hybrid GGCM that combines the strengths of an advanced process-based GGCM, resolving important processes explicitly, with data-driven machine learning components. NeuralCrop is first trained to emulate a competitive GGCM before it is fine-tuned on observational data. We show that NeuralCrop produces projections with accuracy comparable to state-of-the-art GGCMs across site-level and large-scale crop simulations. NeuralCrop can accurately project the interannual yield variability in European wheat regions and the US Corn Belt. Capturing yield anomalies is essential for developing adaptation strategies in the context of climate change. NeuralCrop can more accurately reproduce yield anomalies across various climatic conditions, with particularly notable improvements under drought extremes. For large-scale,

long-term simulations, our approach is orders of magnitude more computationally efficient. Our results show that end-to-end hybrid crop modelling offers more reliable yield projections that are essential for food risk assessments under climate change and intensifying extreme weather events.

## Introduction

Global food systems face intensifying threats from climate change, particularly extreme weather events [1–3]. Accurately assessing the impacts of changing weather and especially extreme event patterns on agricultural productivity is crucial for the development of adaptation strategies to mitigate adverse effects and sustain future food security [4, 5]. Global gridded crop models (GGCMs) are essential tools for projecting the impacts of climate change [6, 7], and are extensively used in downstream analyses (e.g., food security [8, 9], sustainability [10], or economy [11]). Despite decades of development, state-of-the-art GGCMs retain substantial uncertainties in process representations and generally underestimate crop yield losses during extreme weather events [12–16]. Given the projected increases in frequency and magnitude of extreme events in a warming climate [17], and their strong influence on future food security, these limitations present major challenges for the reliability of crop yield projections and food risk assessments [18].

Machine learning (ML) approaches have emerged rapidly in agricultural ecosystem modelling [19–21]. These models are capable of learning complex, nonlinear interactions, which are difficult to explicitly resolve in process-based GGCMs, from observational data (e.g., remote sensing, field measurements, and subnational statistics), providing an alternative for crop yield projections. ML approaches have been successfully used to emulate GGCMs to enable sensitivity and uncertainty analyses under input perturbations [22], and to downscale GGCM outputs to finer spatial and temporal resolutions [23]. Once trained, ML approaches typically require considerably lower computational costs and memory demands during inference than traditional GGCMs.

However, ML approaches have noteworthy limitations compared with GGCMs. Most ML models are optimized using root-mean-squared-error loss, which rewards averaging over uncertainty and consequently produces overly smoothed projections for long-term crop simulations [24]. Lacking realistic biophysical mechanisms, these purely data-driven models only capture statistical correlations, leading to limited interpretability and poor extrapolation to unseen future climates [19, 25]. Ensuring generalization and physical consistency thus remains a primary barrier to the application of pure ML models in crop modelling. In addition, sparse observational data further limits the use of pure ML models [26]. Despite some success in using ML approaches on crop simulations, these models have not demonstrated to outperform state-of-the-art GGCMs [22, 23].

In light of the complementary benefits and limitations of process-based and ML-based models, hybrid models have been proposed as a promising direction for model

development [27, 28]. By replacing or augmenting poorly represented physical processes with data-driven ML components [29, 30], hybrid models have achieved notable success across diverse fields, outperforming pure ML models and traditional process-based models [31–33]. Several studies have recently explored the combination of ML models with GGCs [34–37], but ML in these models is typically used in a post-processing step to adjust outputs from GGCs, or used to emulate these models, rather than being integrated into their internal processes. To enable efficient gradient-based optimization of all parameters jointly and consistently, the hybrid model should support automatic differentiation [29]. However, existing traditional GGCs are not differentiable. A key technical challenge for traditional GGCs in this context is that they are typically written in Fortran or C, which struggle to support automatic differentiation and hinder ML integration into GGCs. This can be solved by using a language that is suitable for both process-based components and ML model training, like Python or Julia.

Here we introduce NeuralCrop, a differentiable hybrid GGC that combines the strengths of the state-of-the-art GGC LPJmL [38] with ML approaches. By implementing components in a differentiable form to achieve seamless integration with ML methods, NeuralCrop enables end-to-end ‘online training’, with ML components optimized in tandem with the model dynamics. Due to sparse observational data, NeuralCrop is first pre-trained on GGC outputs and further fine-tuned using a global network of site-level observations. Extensive benchmarking shows that NeuralCrop significantly outperforms LPJmL in simulating daily carbon and water fluxes across diverse crop sites, and produces yield projections with accuracy comparable to best-in-class GGCs across a range of moisture gradients, with strong improvements under extreme climatic conditions.

## NeuralCrop

NeuralCrop is based on the LPJmL (“Lund-Potsdam-Jena managed Land”) model, which explicitly simulates carbon, water, energy, and nitrogen flows for both natural vegetation and agricultural crops at  $0.5^\circ \times 0.5^\circ$  (latitude  $\times$  longitude) spatial and daily temporal resolution [38–41]. LPJmL is a state-of-the-art process-based GGC and contributes to the global model intercomparison networks AgMIP and ISIMIP [42, 43]. It has been comprehensively evaluated at the global scale [44–47]. In NeuralCrop, neural networks are embedded to replace or augment key biological processes of LPJmL that are uncertain or simplified but directly observable, such as photosynthesis and soil moisture dynamics, or to emulate processes that are heuristic, such as carbon allocation. The considered process-based components within NeuralCrop are fully differentiable to enable a seamless integration with neural networks. These are described in detail in the Supplementary Information B.

Given limited high-quality agricultural observations, we adopt a two-stage strategy to train NeuralCrop, as illustrated in Fig. 1. In the absence of sufficient observational data, pre-training NeuralCrop on extensive LPJmL simulations allows the ML components to learn physically consistent representations, especially for latent variables. This can accelerate and stabilize convergence during subsequent fine-tuning with observational data. End-to-end ‘online training’ allows NeuralCrop to account for interactions

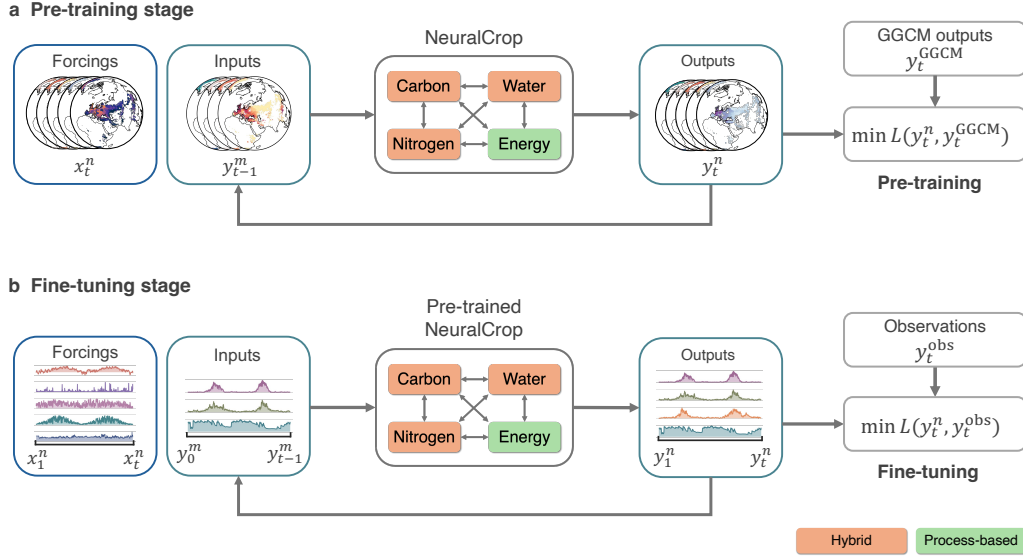


**Fig. 1** Schematic of the NeuralCrop two-stage training framework. It shows how forcings  $x_t^n$ , including weather, soil properties, land use, and field management (e.g., crop calendar, tillage, residue, and fertilizer), and previous time-step model states  $y_{t-1}^m$  are fed into NeuralCrop at each time step  $t$ , where  $n$  denotes the number of forcing variables and  $m$  denotes the number of model states. These model states  $y_{t-1}^m$  are fed into the corresponding neural networks of hybrid components, which advance the evolution of model states over time. The new model states  $y_t^m$  are then fed back into the model to compute the next time step. **a**, In the pre-training stage, NeuralCrop is trained to emulate the behavior of the process-based GGCM LPJmL by minimizing the discrepancies  $L(y_t^n, y_t^{GGCM})$  between NeuralCrop output  $y_t^n$  and LPJmL output  $y_t^{GGCM}$ , given identical weather, soil property, land use, and field management inputs. **b**, In the fine-tuning stage, the pre-trained NeuralCrop is further trained using observational data from eddy-covariance observation networks, which serves as ground truth.

between ML and process-based components in a natural way, ensuring physical consistency in the learned representations [29]. Furthermore, NeuralCrop supports full graphics-processing-unit (GPU) acceleration, which makes global grid-based simulations, and especially large ensembles thereof, computationally much more efficient, in particular above a certain resolution or ensemble size.

We train NeuralCrop models at both the site and regional levels for different crops. The training setup details can be found in the Supplementary Information section D. For site-level representations, we evaluate the ability of NeuralCrop to reproduce daily gross primary productivity (GPP), ecosystem respiration (RECO), net ecosystem exchange (NEE), and soil water content (SWC) against flux tower observations (see Supplementary Information section F). For large-scale cropping regions, we evaluate NeuralCrop’s performance in simulating wheat and maize yields under both normal and extreme climate conditions against reported yield statistics from two major global breadbaskets, i.e., European wheat regions and the US Corn Belt (see Supplementary Information section G).

## Results

### Long-term yield projections

Our evaluation setup focuses on the ability of NeuralCrop to capture the long-term interannual yield variability, which is a key requirement for GGCMs. We compare simulated wheat yields from NeuralCrop and state-of-the-art GGCMs with the harmonized EU subnational crop statistics dataset (hereafter, EU statistics) [48] and corn yields with USDA statistics at the county level over the period 2000-2016. The simulated yields are aggregated from a spatial resolution of  $0.5^\circ$  to the subnational units of yield statistics, using an area-weighted averaging method (see Methods and Supplementary Information H.1). Prior to comparison, we detrend all yield time series using a cubic smoothing spline to remove the effects of long-term crop breeding advances and management improvements, focusing on climate-driven yield variability (Methods and Supplementary Information H.2).

### European wheat

The temporal correlations between simulated and statistical yields for each region over 2000-2016 are shown in Figures 2a-c. LPJmL exhibits strong spatial heterogeneity, with high correlations in Eastern Europe, but weak or even negative values in parts of Western, Central, and Northern Europe (such as many regions of France and Germany). Notably, the ensemble median of AgMIP captures a similar but generally weaker spatial correlation pattern to LPJmL, indicating a common challenge for current GGCMs in the latter regions. In contrast, NeuralCrop presents a more spatially consistent pattern of positive correlations. Figures 2d-e illustrate the spatial distribution of the correlation difference between NeuralCrop and GGCMs (also see Extended Data Fig. 6). Among 800 subnational regions, NeuralCrop achieves higher correlation in 528 regions than LPJmL, accounting for 66%, with 258 regions (32.25%) showing notable improvements where the correlation increases more than 0.2. When compared against the ensemble median of AgMIP, NeuralCrop also demonstrates strong performance in capturing interannual yield variability, achieving higher correlations in 601 regions with 414 regions showing notable improvements (correlation increase exceeding 0.2). At the country level, NeuralCrop outperforms LPJmL (AgMIP) in 16 (19) of the 26 countries (see Extended Data Fig. 6). NeuralCrop shows pronounced improvement in Western and Central Europe, particularly in France and Germany. These regions are consistent with the spatial distribution of eddy-covariance flux observations (see Supplementary Information Fig. S10), suggesting the potential to further improve NeuralCrop’s performance to capture interannual yield variability with more comprehensive observational data.

### US Corn Belt

For the US Corn Belt, we focus on a region including nine states (Supplementary Information Fig. S11), which accounts for about two-thirds of total US corn production [49]. Figures 3a-c show temporal correlations between simulated corn yields and statistical corn yields for each county over the period 2000-2016. LPJmL exhibits

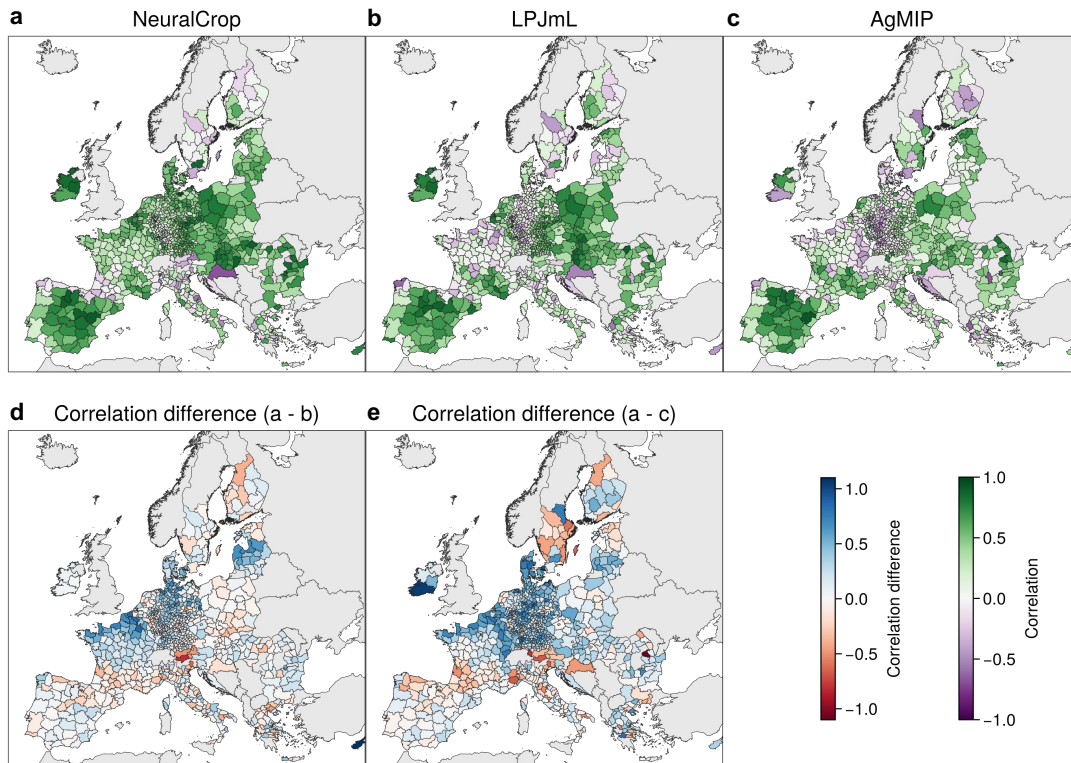


**Fig. 2** Comparison of simulated European wheat yields from NeuralCrop, LPJmL, and the AgMIP ensemble median with EU statistics [48] in European wheat regions. The AgMIP ensemble includes 8 GGCMS. **a**, Time series correlation coefficient between NeuralCrop simulated wheat yield and EU statistics at the subnational level for the period 2000-2016 (range from  $-1$  to  $1$ , darker green areas indicate stronger positive correlations, and darker purple areas indicate stronger negative correlations). **b**, Same as panel a, but for LPJmL. **c**, Same as panel a, but for AgMIP. **d**, The difference of correlation coefficients between NeuralCrop and LPJmL (i.e., panel a – panel b), where blue areas indicate regions where NeuralCrop outperforms LPJmL in simulating interannual yield variability, and red areas indicate regions where LPJmL performs better. NeuralCrop outperforms (underperforms) LPJmL in 66% (34%) of the 800 subnational regions. **e**, Same as panel d but for the difference between NeuralCrop and AgMIP (i.e., panel a – panel c). NeuralCrop outperforms (underperforms) AgMIP in 75.25% (24.75%) of the 800 subnational regions.

strong correlations in the southern US Corn Belt, but weak or even negative values in the north (such as parts of Minnesota, Wisconsin, and Michigan). NeuralCrop is generally more robust than LPJmL and corrects the negative correlations in the northern regions. The AgMIP ensemble demonstrates strong and spatially consistent correlations across the US Corn Belt. Figures 3d-e illustrate the spatial distribution of the correlation difference between NeuralCrop and GGCMS (also see Extended Data Fig. 7). Among 677 counties, NeuralCrop yields higher correlation in 484 counties, accounting for 71.49%, with 185 counties (27.32%) showing remarkable improvements

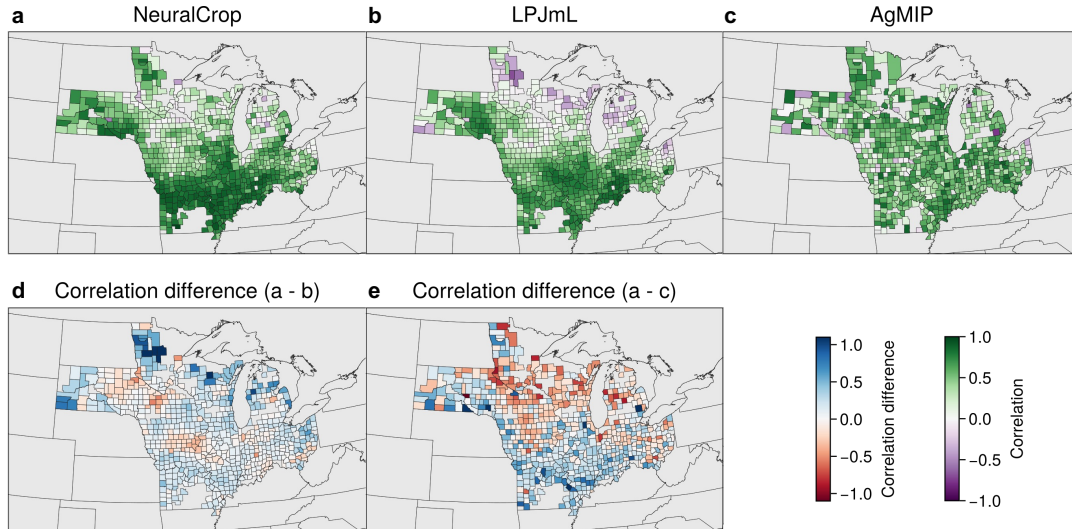


**Fig. 3** Comparison of simulated corn yields from NeuralCrop, LPJmL, and the AgMIP ensemble median with USDA statistics in the US Corn Belt, including nine states (i.e., South Dakota, Minnesota, Iowa, Missouri, Wisconsin, Illinois, Michigan, Indiana, and Ohio). The AgMIP ensemble includes 8 GGCMs. **a**, Time series correlation coefficient between NeuralCrop simulated corn yield and USDA statistics at the county level for the period 2000-2016 (range from  $-1$  to  $1$ , darker green areas indicate stronger positive correlations, and darker purple areas indicate stronger negative correlations). **b**, Same as panel a, but for LPJmL. **c**, Same as panel a, but for AgMIP. **d**, The difference of correlation coefficients between NeuralCrop and LPJmL (i.e., panel a – panel b), where blue areas indicate regions where NeuralCrop outperforms LPJmL in simulating interannual yield variability, and red areas indicate regions where LPJmL performs better. NeuralCrop outperforms (underperforms) LPJmL in 71.49% (28.51%) of the 677 counties. **e**, Same as panel d but for the difference between NeuralCrop and AgMIP (i.e., panel a – panel c). NeuralCrop outperforms (underperforms) AgMIP in 53% (47%) of the 677 counties.

where correlation increases more than 0.2. When compared against the ensemble median of AgMIP, NeuralCrop achieves higher correlations in 422 regions with 150 regions showing notable improvements (correlation increase exceeding 0.2). At the country level, NeuralCrop outperforms LPJmL (AgMIP) in 7 (5) of the 9 states (see Extended Data Fig. 7). NeuralCrop underperforms the AgMIP ensemble in the northern regions. It is noted that no single GGCM consistently outperforms the others, as individual model performance varies significantly across crop types and geographical regions. Multi-model ensembles are the primary strategy for mitigating uncertainties in crop simulations [16]. NeuralCrop demonstrates that hybrid crop modelling has great potential to enhance its base model performance. We expect that applying this approach to state-of-the-art GGCMs will significantly improve the projecting performance of multi-model ensembles.

## Performance across moisture gradients

We evaluate the ability of NeuralCrop to reproduce yield anomalies (Supplementary Information H.3) across the European wheat regions and the US Corn Belt over the period 2000–2016, under various moisture gradients as defined by the respective growing-season Standardized Precipitation Evapotranspiration Index (SPEI). The SPEI is a drought index used to characterize drought intensity, duration, and frequency across different timescales [50] (Supplementary Information G.4). We use April–June SPEI for wheat and May–July SPEI for corn [51–53]. We further select two specific drought years as case studies, i.e., the 2018 European drought and the 2012 US drought, to evaluate the performance of NeuralCrop under extreme drought events. All analyses are based on detrended yield data (Methods and Supplementary Information H.2).

## Yield anomalies across years

It is evident that NeuralCrop outperforms LPJmL and the AgMIP ensemble in capturing yield anomalies for both wheat and corn across various moisture gradients (Fig. 4). Under dry conditions, the yield statistics (benchmark) reveal that both wheat and corn yields decline significantly as drought intensifies (Fig. 4a). While LPJmL and AgMIP capture the general trend of increasing yield losses, they show a tendency to underestimate drought-induced yield losses, consistent with previous findings [16, 54]. NeuralCrop generally achieves the lowest root mean square error (RMSE) and matches the benchmark medians and means more closely across all dryness classes. Under wet conditions, the benchmark shows that wheat yields experience amplified losses as wetness intensifies, whereas LPJmL and AgMIP erroneously project a trend of yield increases (Fig. 4b), indicating the limitations of state-of-the-art GGCMs in representing waterlogging stress. This likely stems from the fact that current GGCMs do not explicitly simulate the impacts of water excess on crops, which limits their ability to reproduce yield anomalies across wetness gradients [55]. NeuralCrop effectively mitigates these spurious yield gains, achieving the lowest RMSE and matching the benchmark medians and means more closely across all wetness classes. These results suggest that NeuralCrop provides a more consistent and accurate representation of yield responses across moisture gradients, particularly under extreme conditions where existing GGCMs show systematic limitations.

## Case study

As extreme weather events are expected to increase in frequency and magnitude due to climate change [17], an important ability of GGCMs is to project yield anomalies under extreme events. Fig. 5 shows a case study that illustrates the performance of NeuralCrop during the 2018 European drought and the 2012 US drought. It is noted that the AgMIP wheat ensemble is excluded from this analysis as it only provides historical yield simulations up to 2016, and the AgMIP corn ensemble is presented in Extended Data Fig. 8. Fig. 5a shows that the majority of Europe experienced significant drought-induced wheat yield losses in 2018, especially regions in Central and Northern Europe. Similarly, most of the US Corn Belt suffered from severe corn yield

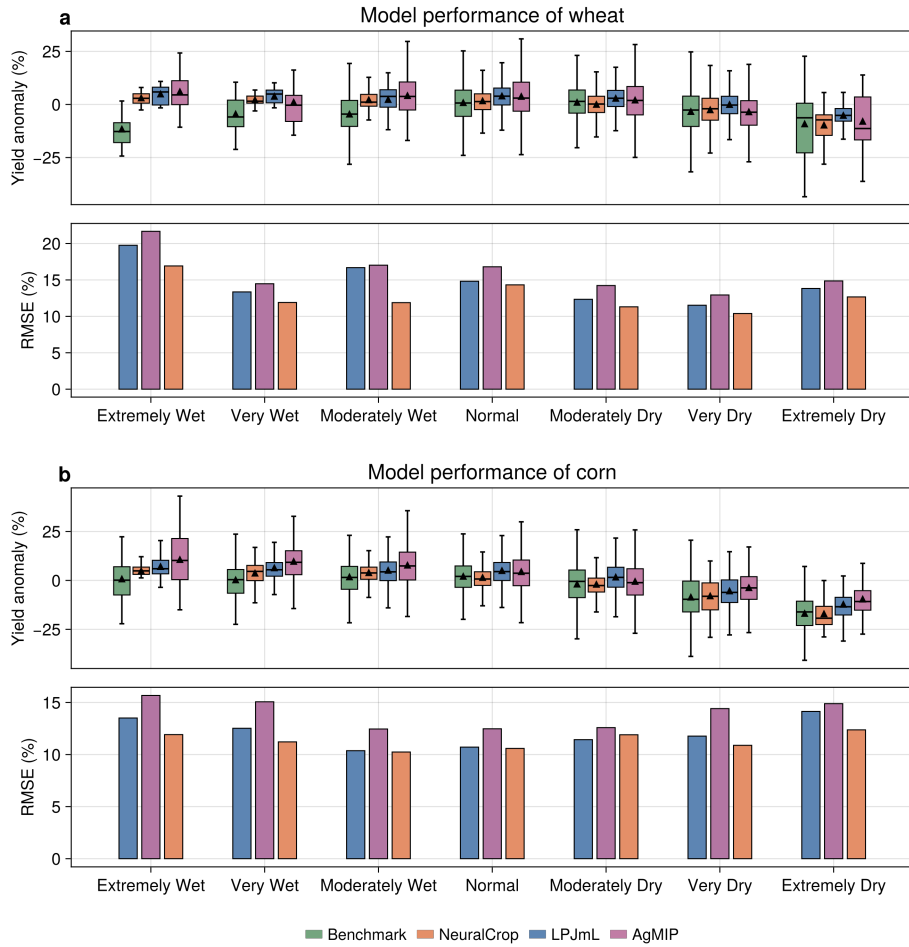


**Fig. 4** Comparison of simulated yield anomalies from NeuralCrop, LPJmL, and the AgMIP ensemble median with yield statistics (benchmark) for European wheat and US Corn Belt across moisture gradients at the subnational level during 2000–2016. The AgMIP ensemble includes 8 GGCMs. **a**, The boxplots represent the reported and simulated wheat yield anomalies in the EU over the period 2000–2019, grouped by the April–June Standardized Precipitation Evapotranspiration Index (SPEI, see Supplementary Information G.4). Green boxes denote EU statistics, orange boxes denote NeuralCrop, blue boxes denote LPJmL, and purple boxes denote AgMIP. The box boundaries represent the interquartile range (IQR), defined by the first quartile, the median, and the third quartile. The upper and lower whiskers represent the maximum and minimum values that are within 1.5 times the interquartile range of the box. The black triangles are the mean values. The bars in the lower panel represent the root mean square error (RMSE) for NeuralCrop, LPJmL, and AgMIP within each SPEI class. Orange bars denote NeuralCrop, blue bars denote LPJmL, and purple bars denote AgMIP. **b**, Same as panel a, but for corn yields evaluated against USDA statistics.

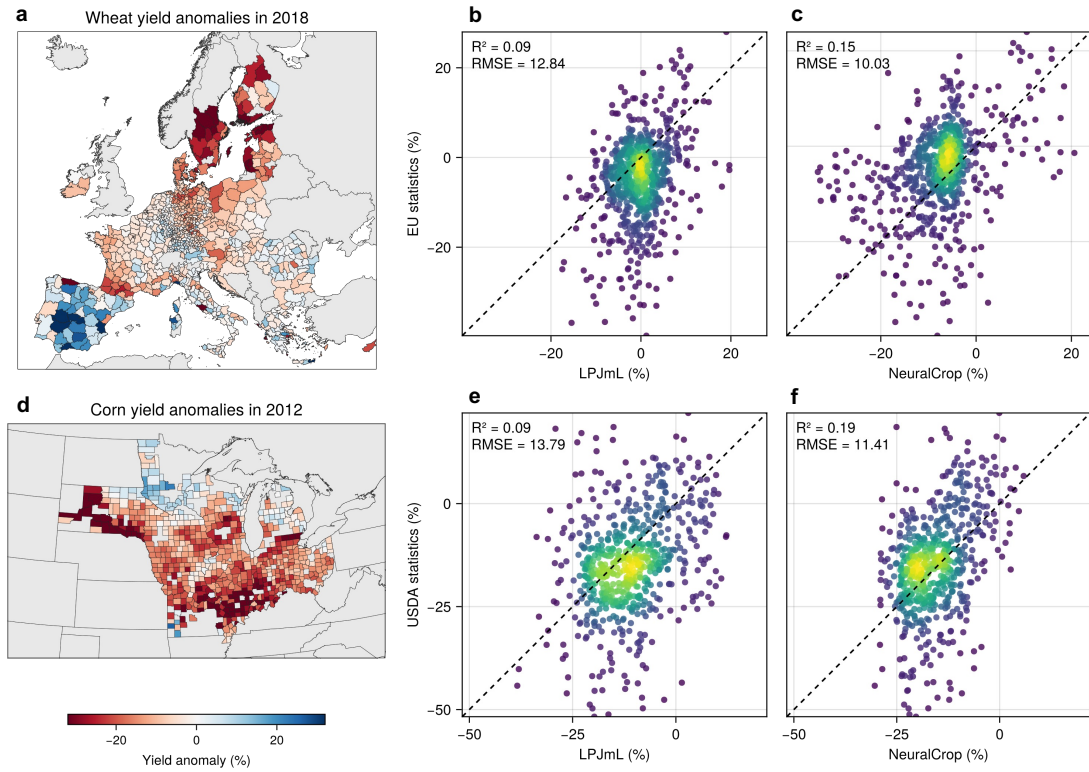


**Fig. 5** Yield anomalies and model performance for NeuralCrop and LPJmL under the extreme drought years. **a**, Wheat yield anomalies in 2018 at the subnational level from EU statistics. **b**, Scatter plot comparing simulated wheat yield anomalies (%) by LPJmL against EU statistics (benchmark). The color gradient indicates the density of data points, and the dashed line represents the 1:1 line.  $R^2$  and RMSE values are shown in the upper left. **c**, Same as panel **b**, but for NeuralCrop. **d**, Corn yield anomalies in 2012 at the county level from USDA statistics. **e**, Scatter plot comparing simulated corn yield anomalies (%) by LPJmL against USDA statistics (benchmark). **f**, Same as panel **e**, but for NeuralCrop.

deficits in 2012 (Fig. 5d). LPJmL generally underestimates the extent of yield losses for both the 2018 wheat and 2012 corn drought events, but NeuralCrop outperforms the process-based LPJmL in capturing these negative yield anomalies with higher  $R^2$  and lower RMSE, despite slightly overestimating these deficits. When compared to the AgMIP corn ensemble (Fig. 8), NeuralCrop also achieves higher  $R^2$  and lower RMSE. As drought and heat typically occur together, we further investigate their compound impacts on yield anomalies. We find that the maximum temperature during the growing season intensified the impact of drought on yield anomalies for both wheat and corn (see Supplementary Information Fig. S16 and Fig. S17). NeuralCrop also demonstrates a stronger performance in capturing these compounding impacts.

## Discussion

NeuralCrop can more accurately reproduce the daily and seasonal dynamics of carbon and water fluxes across diverse crop in-situ observation sites (Supplementary Information F). The interannual instability of crop yields is a critical determinant of food security under climate change [56], which is a key indicator for evaluating the performance of GGCMs. Traditional GGCMs suffer from pronounced spatial heterogeneity in yield-projection accuracy, which poses a major challenge for global food risk assessments. NeuralCrop exhibits more accurate projections of the interannual yield variability at European wheat regions and the US Corn Belt after fine-tuning with site-level observations. We believe NeuralCrop has the potential to improve simulations when more observations are available. Traditional GGCMs can typically detect but underestimate the drought-induced yield losses across various drought conditions [57], and fail to capture the yield losses driven by wet extremes. Our results show that NeuralCrop outperforms GGCMs in capturing yield anomalies across various moisture gradients with higher fidelity for both wheat and maize. Overall, NeuralCrop shows that incorporating ML is a promising approach for reducing uncertainty in process representations and parameterizations within GGCMs.

NeuralCrop is, to our knowledge, the first hybrid, end-to-end 'online' trainable GGCM that combines the strengths of state-of-the-art GGCMs with ML approaches. Compared with 'offline' training, where the ML component is trained independently of the evolving model states, end-to-end 'online' training enables ML components within NeuralCrop to continuously learn from and adjust the evolving model states. This co-evolution ensures that NeuralCrop maintains numerical stability over long-term simulations, preventing error accumulation [32], and also improves physical consistency. Compared with traditional GGCMs, NeuralCrop is computationally orders of magnitude more efficient. For example, running NeuralCrop on a single GPU and LPJmL on 128 central-processing-unit (CPU) cores at  $0.5^\circ$  spatial resolution with daily time steps over 20 years, respectively, NeuralCrop achieved up to an  $82.3\times$  speedup as the number of grid cells increased to 14,157 (see Extended Data Fig. 9 and Supplementary Information Table. S4). This can be used for previously impractical tasks such as large ensemble simulations.

Pure ML approaches for crop modelling typically struggle to generalize to unseen data [19]. Due to its hybrid approach, NeuralCrop demonstrates robust out-of-sample generalization capabilities (see Supplementary Information section G.3). We expect that it can be used to accurately simulate data-sparse, climate-vulnerable, and under-studied cropping regions, for example in Africa, South America, and Asia. Furthermore, as individual GGCM performance varies significantly across crops and regions, multi-model ensembles remain essential for mitigating simulation uncertainties [16]. NeuralCrop demonstrates that hybrid crop modelling has great potential to enhance its base model performance. When applying this approach to state-of-the-art GGCMs, substantial headroom exists to further improve the projecting performance of multi-model ensembles.

Due to limited understanding, many biophysical processes are oversimplified or omitted in GGCMs [58]. For instance, the representation of soil waterlogging remains in its infancy in advanced GGCMs, and many GGCMs including LPJmL do not

account for soil waterlogging mechanisms [55], consistent with our results that yield responses under wet extremes are poorly captured by GGCs. Similarly, processes like the impacts of compound climate events and pest/disease stress are only partially simulated or not included in traditional GGCs [12]. These gaps limit the ability of GGCs to simulate the individual and combined effects of these stresses. As an example, LPJmL failed to detect the yield losses driven by heavy rainfall in combination with soil anoxia and diseases in central and northern France in 2016, and instead projected a yield increase (Supplementary Information Fig. S18) [51, 59]. While pre-trained NeuralCrop inherits the same process limitations, it captures part of the negative but smaller yield anomalies in northern France after fine-tuning (Supplementary Information Figs. S18c-f). This suggests that, despite without an explicit representation of these processes, the ML components can still learn from observational data to partially capture their indirect impacts.

NeuralCrop is flexible to incorporate new process knowledge as our understanding of crop biophysical processes advances or with more ML components as higher-quality observational data becomes available. It also provides a powerful means to diagnose what processes are not well represented in the original GGCs. Until now, the high-quality observational data suitable for the NeuralCrop training comes from eddy-covariance observation networks. In regions where more data is available, results showed that NeuralCrop strongly outperforms traditional GGCs. We hence expect that end-to-end 'online training', with observational data covering broader areas and longer time periods, will enable more realistic crop simulations. Given ongoing climate change, more advanced and climate-robust GGCs are needed to quantify the impacts of climate change and especially intensifying extreme weather events on agricultural productivity. We believe the hybrid modelling approach of NeuralCrop offers a promising avenue to support food risk assessments.

## Methods

### Pre-training data generation

We use LPJmL to generate data to pre-train NeuralCrop. The process-based LPJmL model simulates global carbon, water, and nitrogen fluxes and stocks, and surface energy balance for both natural vegetation and agricultural crops [38–41]. As a contributing model to the global model intercomparison networks AgMIP and ISIMIP, LPJmL has been comprehensively evaluated at the global scale [42, 43, 45, 47]. For cropland, driven by climate forcing, soil properties, land use, and field management (e.g., crop calendar, tillage, residue, and fertilizer), LPJmL simulates key biophysical processes such as photosynthesis, carbon allocation, evapotranspiration, and soil moisture dynamics, as well as bioclimatic impacts on crop growth, development, yield formation across different crop functional types [39].

We ran LPJmL (version 5) on a global grid at  $0.5^\circ \times 0.5^\circ$  (latitude  $\times$  longitude) spatial and daily temporal resolution [40]. An initial 5000-year spin-up simulation under potential natural vegetation (i.e., without land use) was performed to bring soil carbon, nitrogen, and water pools into dynamic equilibrium. Starting from these equilibrium states, a second 390-year spin-up simulation was conducted to introduce the

impacts of historical land-use change on these pools. Both spin-up simulations used the first 30-year climate data cycled repeatedly to force LPJmL. The resulting model states ensure biophysically consistent initial conditions for subsequent transient simulations of crop growth. The detailed description can be found in the Supplementary Information section C.

## NeuralCrop architecture

NeuralCrop explicitly resolved key processes, following their representation in the LPJmL model, and is rewritten to support automatic differentiation and GPU optimization, using the Julia programming language. NeuralCrop embeds ML components, here fully-connected neural networks, into the process-based crop model to replace or augment components that are uncertain or simplified (Supplementary Information B). Neural networks can theoretically be used to parameterize any biased or simplified process-based components within GCMs [27]. In practice, however, their applicability is constrained by the availability of observational data for training. It is only feasible to combine neural networks with process-based components whose prognostic variables are observable. In agricultural ecosystems, high-quality observational data remain scarce. While numerous remote sensing data is now available, their spatiotemporal resolutions are heterogeneous, making it difficult to use these data to train hybrid models [12]. Currently, global eddy-covariance observation networks (e.g., FLUXNET [60] and AmeriFlux [61]) provide continuous, high-quality daily observations of crop carbon and water fluxes. Training on these data allows neural networks to improve the representation of carbon and soil water-related processes in GCMs. We described in detail in Supplementary Information B how key process-based components, i.e., photosynthesis, carbon allocation, soil carbon and nitrogen decomposition, and soil water dynamics, are combined with neural networks.

The considered process-based components of NeuralCrop are implemented in a fully differentiable manner to enable the end-to-end 'online training', which requires all processes along the backpropagation path to be differentiable by automatic differentiation (AD) [62]. Differentiability allows ML components to be optimized by taking into account interactions with the governing equations for model dynamics. For example, we use neural ordinary differential equations (NODE) [63] in NeuralCrop to emulate daily carbon allocation (described in Supplementary Information B.2). Through 'online training', the NODE parameters are updated while accounting for interactions with internal prognostic states. Another big advantage of differentiability is that unobservable latent variables parameterized by neural networks can be implicitly optimized through backpropagation using target prognostic observations. For example, in NeuralCrop, we use two fully-connected neural networks to parameterize two latent variables in photosynthesis (i.e.,  $\lambda$ , a key variable related to photosynthetic electron transport capacity, and maximum photosynthetic carboxylation rate  $V_{cmax}$ ), respectively (described in Supplementary Information B.1). This approach enables NeuralCrop to capture the spatiotemporal variability of both  $\lambda$  and  $V_{cmax}$  using target GPP data, thereby reducing uncertainty in the representation of photosynthesis.

NeuralCrop is implemented in Julia [64], a high-performance and mature programming language for numerical and scientific computing, and its differentiability is

supported by the automatic differentiation package Zygote.jl [65]. NeuralCrop is initialized using equilibrium states of soil carbon, nitrogen, and water pools generated from LPJmL simulations. All climate inputs to neural networks are standardized to a normal distribution with zero mean and unit variance, while prognostic variable inputs are linearly scaled to the range  $[0, 1]$  using their physical limits. NeuralCrop is optimized for GPUs, which is computationally efficient due to its neural-network components and grid-based simulations.

## Two-stage training approach

Due to the limited high-quality observational data, we adopt a two-stage training approach to train NeuralCrop at  $0.5^\circ \times 0.5^\circ$  (latitude  $\times$  longitude) spatial and daily temporal resolution (Fig. 1). During the pre-training stage, we train NeuralCrop on LPJmL outputs using a loss function composed of two terms (Supplementary Information D.3, Eq. S24). The first loss term promotes predictive accuracy by minimizing discrepancies between NeuralCrop projections and LPJmL outputs, while the second loss term imposes physical constraints to obey carbon mass balance. We then fine-tune the pre-trained model using real-world observations, specifically the carbon and water flux data from eddy-covariance observation networks, using the accuracy loss function (Supplementary Information D.3, Eq. S25). The processing of flux data is described in detail in Supplementary Information C.4. The fine-tuning adjusts the model to better match observed carbon and water dynamics by correcting biases inherited from LPJmL. All model outputs used for training are normalized by their respective maximum value computed prior to model initialization, and all loss terms are defined using the standard mean squared error (MSE) (Supplementary Information D.3, Eq. S23).

We use a rollout length that covers the entire crop growing period (from sowing to harvest) to both pre-train and fine-tune NeuralCrop, which we find enables stable and robust model training (Supplementary Information D.5). Although shorter rollouts offer higher training efficiency, they often lead to loss oscillation and convergence failures. This instability becomes more pronounced as the rollout length decreases, highlighting the importance of incorporating the entire crop growing period into each training rollout. We set a 365-day rollout as the default to train all NeuralCrop models in our study.

## Data sources and benchmarking

We select European wheat regions and the US Corn Belt over the period 2000-2016 to evaluate the performance of NeuralCrop under both normal and extreme climate conditions. These two large-scale cropping regions are selected because of their long-term, high-quality eddy-covariance observations for fine-tuning, as well as annual subnational crop yield statistics for evaluation. Yield data used for evaluation are publicly available from the harmonized European Union subnational crop statistics dataset [48] and the USDA-NASS database, as described in Supplementary Information G.1.1 and G.2.1. It's noted that these two datasets are the most reliable yield statistics from these regions but may not fully represent ground-truth yields, as they are subject to potential errors due to reporting inaccuracies. The yield

simulations from the other 8 GGCMS, including ACEA [66], CROVER [67], EPIC-IIASA [68], ISAM [69], LDNDC [70], LPJ-GUESS [71], PEPIC [72], pDSSAT [73], and SIMPLACE-LINTUL5 [74], are accessible from AgMIP GGCMI Phase 3, providing historical yield simulations up to 2016.

## Yield data processing

We aggregate simulated yields to the corresponding subnational unit of reported yield statistics (primarily NUTS-3 level in EU countries, and county level in the US) using an area-weighted averaging method, respectively, as described in Supplementary Information H.1. In European wheat regions, spring and winter wheat are simulated under rain-fed and irrigated management conditions, which are jointly evaluated against reported total wheat yields, including soft and durum wheat. In the US Corn Belt, the corn is simulated under rain-fed and irrigated management conditions to compare with reported corn yields. Prior to comparison, both simulated and reported yield time series are detrended using a cubic smoothing spline to remove the effects of long-term crop breeding advances and management improvements, thereby isolating the inter-annual variability primarily driven by climate change, described in Supplementary Information H.2.

## Evaluation metrics

For interannual yield variability, we use the Pearson correlation coefficient (Supplementary Information section E.1) as a metric to evaluate the model performance. For yield anomalies, we use root mean square error (RMSE) (Supplementary Information section E.3), or the coefficient of determination ( $R^2$ , see Eq. S28), i.e., the squared Pearson correlation coefficient (Supplementary Information section E.2) as the evaluation metrics.

## Data availability

For running LPJmL and training NeuralCrop, we used the bias-corrected climate inputs from ISIMIP3a GSWP3-W5E5 datasets for the period 1901–2019, which are publicly available for download at <https://www.isimip.org/>. The data for cultivated area fraction and annual fertilizer rates were obtained from the LUH2v2 dataset [75]. The crop residue data were accessed from ref. [76]. The crop tillage management data were obtained from ref. [77]. Soil properties (e.g., soil textures and pH) and crop sowing dates were accessed from Agricultural Model Intercomparison and Improvement Project (AgMIP) [45].

The flux data used to finetune NeuralCrop were obtained from the global flux network FLUXNET2015 (<https://fluxnet.org/data/fluxnet2015-dataset/>) and FLUXNET-CH4 (<https://fluxnet.org/data/fluxnet-ch4-community-product/>), the American flux network AmeriFlux (<https://ameriflux.lbl.gov/data/flux-data-products/>), and the European Integrated Carbon Observation System (ICOS) (<https://www.icos-cp.eu/data-products/>).

The European subnational wheat statistics were downloaded from <https://data.jrc.ec.europa.eu/dataset/685949ff-56de-4646-a8df-844b5bb5f835>, which provides annual wheat (including soft and durum wheat) statistics on area, production, and average yield across three levels of the Nomenclature of Territorial Units for Statistics (NUTS). The subnational corn statistics of the US Corn Belt were obtained from <https://quickstats.nass.usda.gov/>. The yield simulations from the other GCMs are available at <https://www.isimip.org/>.

## Code availability

The NeuralCrop Julia code will be available on GitHub when this work gets published.

## Supplementary information

The manuscript is accompanied by Supplementary Information that describes in detail how to develop, train, and validate NeuralCrop, as well as additional results.

## Author contribution

Y.L., S.B., M.B., M.G., P.H. and N.B. conceived and designed the study. Y.L. wrote the model code, processed the data, trained the models and analysed the results. J.H. provided the yield comparison code. All authors discussed the results. Y.L. wrote the manuscript with contributions from all authors.

## Acknowledgements

Y.L. acknowledges funding from the program of the China Scholarship Council (no.202303250017). N.B. and S.B. acknowledge funding from the Volkswagen Foundation. This is ClimTip contribution #X; the ClimTip project has received funding from the European Union's Horizon Europe research and innovation programme under grant agreement no.101137601. The authors gratefully acknowledge the Ministry of Research, Science and Culture (MWFK) of Land Brandenburg for supporting this project by providing resources on the high performance computer system at the Potsdam Institute for Climate Impact Research.

## References

- [1] Yang, Y., Tilman, D., Jin, Z., Smith, P., Barrett, C.B., Zhu, Y.-G., Burney, J., D’Odorico, P., Fantke, P., Fargione, J., *et al.*: Climate change exacerbates the environmental impacts of agriculture. *Science* **385**(6713), 3747 (2024)
- [2] Rezaei, E.E., Webber, H., Asseng, S., Boote, K., Durand, J.L., Ewert, F., Martre, P., MacCarthy, D.S.: Climate change impacts on crop yields. *nature reviews earth & environment* **4**(12), 831–846 (2023)
- [3] Hasegawa, T., Sakurai, G., Fujimori, S., Takahashi, K., Hijioka, Y., Masui, T.: Extreme climate events increase risk of global food insecurity and adaptation needs. *Nature Food* **2**(8), 587–595 (2021)
- [4] Hultgren, A., Carleton, T., Delgado, M., Gergel, D.R., Greenstone, M., Houser, T., Hsiang, S., Jina, A., Kopp, R.E., Malevich, S.B., *et al.*: Impacts of climate change on global agriculture accounting for adaptation. *Nature* **642**(8068), 644–652 (2025)
- [5] Lesk, C., Rowhani, P., Ramankutty, N.: Influence of extreme weather disasters on global crop production. *Nature* **529**(7584), 84–87 (2016)
- [6] Jägermeyr, J., Müller, C., Ruane, A.C., Elliott, J., Balkovic, J., Castillo, O., Faye, B., Foster, I., Folberth, C., Franke, J.A., *et al.*: Climate impacts on global agriculture emerge earlier in new generation of climate and crop models. *Nature Food* **2**(11), 873–885 (2021)
- [7] Adrian, R., Craig, M., Degvold, F., Ebi, K.L., Frieler, K., Jamshed, A., McMillan, J., Mechler, R., New, M., Simpson, N., *et al.*: Climate change 2022-impacts, adaption and vulnerability. summary for policymakers (2022)
- [8] Beier, F.D., Dietrich, J.P., Heinke, J., Abrahao, G., Jeetze, P., Bodirsky, B.L., *et al.*: Planetary boundaries under a land-based climate change mitigation scenario with a food demand transformation: a modelling study. *The Lancet Planetary Health* **9**(10), 101249 (2025) [https://doi.org/10.1016/S2542-5196\(25\)00087-7](https://doi.org/10.1016/S2542-5196(25)00087-7)
- [9] Luchtenbelt, H., Doelman, J., Bos, A., Daioglou, V., Jägermeyr, J., Müller, C., Stehfest, E., Vuuren, D.: Quantifying food security and mitigation risks consequential to climate change impacts on crop yields. *Environmental Research Letters* **20**(1), 014001 (2024)
- [10] Kahiluoto, H., Sakieh, Y., Kaseva, J., Kersebaum, K.-C., Minoli, S., Franke, J., Rötter, R.P., Müller, C.: Redistribution of nitrogen to feed the people on a safer planet. *PNAS nexus* **3**(5), 170 (2024)
- [11] Orlov, A., Jägermeyr, J., Müller, C., Daloz, A.S., Zabel, F., Minoli, S., Liu, W., Lin, T.-S., Jain, A.K., Folberth, C., *et al.*: Human heat stress could offset potential

- economic benefits of co2 fertilization in crop production under a high-emissions scenario. *One Earth* **7**(7), 1250–1265 (2024)
- [12] Wang, B., Jägermeyr, J., O’Leary, G.J., Wallach, D., Ruane, A.C., Feng, P., Li, L., Liu, D.L., Waters, C., Yu, Q., *et al.*: Pathways to identify and reduce uncertainties in agricultural climate impact assessments. *Nature Food* **5**(7), 550–556 (2024)
- [13] Xiong, W., Asseng, S., Hoogenboom, G., Hernandez-Ochoa, I., Robertson, R., Sonder, K., Pequeno, D., Reynolds, M., Gerard, B.: Different uncertainty distribution between high and low latitudes in modelling warming impacts on wheat. *Nature Food* **1**(1), 63–69 (2020)
- [14] Asseng, S., Ewert, F., Rosenzweig, C., Jones, J.W., Hatfield, J.L., Ruane, A.C., Boote, K.J., Thorburn, P.J., Rötter, R.P., Cammarano, D., *et al.*: Uncertainty in simulating wheat yields under climate change. *Nature climate change* **3**(9), 827–832 (2013)
- [15] Müller, C., Jägermeyr, J., Franke, J.A., Ruane, A.C., Balkovic, J., Ciais, P., Dury, M., Falloon, P., Folberth, C., Hank, T., Hoffmann, M., Izaurralde, R.C., Jacquemin, I., Khabarov, N., Liu, W., Olin, S., Pugh, T.A.M., Wang, X., Williams, K., Zabel, F., Elliott, J.W.: Substantial Differences in Crop Yield Sensitivities Between Models Call for Functionality-Based Model Evaluation. *Earth’s Future* **12**(3), 2023–003773 (2024) <https://doi.org/10.1029/2023EF003773>
- [16] Iizumi, T., Sakai, T.: The global dataset of historical yields for major crops 1981–2016. *Scientific Data* **7**(1), 97 (2020)
- [17] Lee, H., Calvin, K., Dasgupta, D., Krinner, G., Mukherji, A., Thorne, P., Trisos, C., Romero, J., Aldunce, P., Barrett, K., *et al.*: IPCC, 2023: Climate Change 2023: Synthesis Report. Contribution of Working Groups I, II and III to the Sixth Assessment Report of the Intergovernmental Panel on Climate Change, (2023)
- [18] Koehler, A.-K.: Uncertainties in global crop modelling. *Nature Food* **1**(1), 19–20 (2020)
- [19] Sweet, L.-b., Athanasiadis, I.N., Bree, R., Castellano, A., Martre, P., Paudel, D., Ruane, A.C., Zscheischler, J.: Transdisciplinary coordination is essential for advancing agricultural modeling with machine learning. *One Earth* **8**(4) (2025)
- [20] Liu, L., Zhou, W., Guan, K., Peng, B., Xu, S., Tang, J., Zhu, Q., Till, J., Jia, X., Jiang, C., *et al.*: Knowledge-guided machine learning can improve carbon cycle quantification in agroecosystems. *Nature communications* **15**(1), 357 (2024)
- [21] Van Klompenburg, T., Kassahun, A., Catal, C.: Crop yield prediction using machine learning: A systematic literature review. *Computers and electronics in agriculture* **177**, 105709 (2020)

- [22] Liu, W., Ye, T., Müller, C., Jägermeyr, J., Franke, J.A., Stephens, H., Chen, S.: The statistical emulators of gcmi phase 2: responses of year-to-year variation of crop yield to co<sub>2</sub>, temperature, water, and nitrogen perturbations. *Geoscientific Model Development* **16**(23), 7203–7221 (2023)
- [23] Folberth, C., Baklanov, A., Balkovič, J., Skalský, R., Khabarov, N., Obersteiner, M.: Spatio-temporal downscaling of gridded crop model yield estimates based on machine learning. *Agricultural and forest meteorology* **264**, 1–15 (2019)
- [24] Terven, J., Cordova-Esparza, D.-M., Romero-González, J.-A., Ramírez-Pedraza, A., Chávez-Urbiola, E.: A comprehensive survey of loss functions and metrics in deep learning. *Artificial Intelligence Review* **58**(7), 195 (2025)
- [25] Paudel, D., De Wit, A., Boogaard, H., Marcos, D., Osinga, S., Athanasiadis, I.N.: Interpretability of deep learning models for crop yield forecasting. *Computers and Electronics in Agriculture* **206**, 107663 (2023)
- [26] Tseng, G., Kerner, H., Nakalembe, C., Becker-Reshef, I.: Learning to predict crop type from heterogeneous sparse labels using meta-learning. In: *Proceedings of the IEEE/CVF Conference on Computer Vision and Pattern Recognition*, pp. 1111–1120 (2021)
- [27] Reichstein, M., Camps-Valls, G., Stevens, B., Jung, M., Denzler, J., Carvalhais, N., Prabhat, F.: Deep learning and process understanding for data-driven earth system science. *Nature* **566**(7743), 195–204 (2019)
- [28] Irrgang, C., Boers, N., Sonnewald, M., Barnes, E.A., Kadow, C., Staneva, J., Saynisch-Wagner, J.: Towards neural earth system modelling by integrating artificial intelligence in earth system science. *Nature Machine Intelligence* **3**(8), 667–674 (2021)
- [29] Gelbrecht, M., White, A., Bathiany, S., Boers, N.: Differentiable programming for earth system modeling. *Geoscientific Model Development* **16**(11), 3123–3135 (2023)
- [30] Shen, C., Appling, A.P., Gentine, P., Bandai, T., Gupta, H., Tartakovsky, A., Baity-Jesi, M., Fenicia, F., Kifer, D., Li, L., *et al.*: Differentiable modelling to unify machine learning and physical models for geosciences. *Nature Reviews Earth & Environment* **4**(8), 552–567 (2023)
- [31] Liu, Y., Huang, H., Wang, S.-C., Zhang, T., Xu, D., Chen, Y.: Elm2. 1-xgbfire1. 0: improving wildfire prediction by integrating a machine learning fire model in a land surface model. *Geoscientific Model Development* **18**(13), 4103–4117 (2025)
- [32] Kochkov, D., Yuval, J., Langmore, I., Norgaard, P., Smith, J., Mooers, G., Klöwer, M., Lottes, J., Rasp, S., Düben, P., *et al.*: Neural general circulation models for weather and climate. *Nature* **632**(8027), 1060–1066 (2024)

- [33] Zhang, C., Perezhogin, P., Gultekin, C., Adcroft, A., Fernandez-Granda, C., Zanna, L.: Implementation and evaluation of a machine learned mesoscale eddy parameterization into a numerical ocean circulation model. *Journal of Advances in Modeling Earth Systems* **15**(10), 2023–003697 (2023)
- [34] Bloh, M., Lobell, D., Asseng, S.: Knowledge informed hybrid machine learning in agricultural yield prediction. *Computers and Electronics in Agriculture* **227**, 109606 (2024)
- [35] Droutsas, I., Challinor, A.J., Deva, C.R., Wang, E.: Integration of machine learning into process-based modelling to improve simulation of complex crop responses. *in silico Plants* **4**(2), 017 (2022)
- [36] Maestrini, B., Mimić, G., Oort, P.A., Jindo, K., Brdar, S., Athanasiadis, I.N., Evert, F.K.: Mixing process-based and data-driven approaches in yield prediction. *European Journal of Agronomy* **139**, 126569 (2022)
- [37] Shahhosseini, M., Hu, G., Huber, I., Archontoulis, S.V.: Coupling machine learning and crop modeling improves crop yield prediction in the us corn belt. *Scientific reports* **11**(1), 1606 (2021)
- [38] Schaphoff, S., Bloh, W., Rammig, A., Thonicke, K., Biemans, H., Forkel, M., Gerten, D., Heinke, J., Jägermeyr, J., Knauer, J., *et al.*: LPJmL4—a dynamic global vegetation model with managed land—part 1: Model description. *Geoscientific Model Development* **11**(4), 1343–1375 (2018)
- [39] Bondeau, A., Smith, P.C., Zaehle, S., Schaphoff, S., Lucht, W., Cramer, W., Gerten, D., LOTZE-CAMPEN, H., Müller, C., Reichstein, M., *et al.*: Modelling the role of agriculture for the 20th century global terrestrial carbon balance. *Global Change Biology* **13**(3), 679–706 (2007)
- [40] Bloh, W., Schaphoff, S., Müller, C., Rolinski, S., Waha, K., Zaehle, S.: Implementing the nitrogen cycle into the dynamic global vegetation, hydrology, and crop growth model lpjml (version 5.0). *Geoscientific Model Development* **11**(7), 2789–2812 (2018)
- [41] Lutz, F., Herzfeld, T., Heinke, J., Rolinski, S., Schaphoff, S., Von Bloh, W., Stoorvogel, J.J., Müller, C.: Simulating the effect of tillage practices with the global ecosystem model lpjml (version 5.0-tillage). *Geoscientific Model Development* **12**(6), 2419–2440 (2019)
- [42] Franke, J.A., Müller, C., Elliott, J., Ruane, A.C., Jägermeyr, J., Balkovic, J., Ciais, P., Dury, M., Falloon, P.D., Folberth, C., *et al.*: The ggcmi phase 2 experiment: global gridded crop model simulations under uniform changes in co<sub>2</sub>, temperature, water, and nitrogen levels (protocol version 1.0). *Geoscientific Model Development* **13**(5), 2315–2336 (2020)

- [43] Frieler, K., Volkholz, J., Lange, S., Schewe, J., Mengel, M., Rocío Rivas López, M., Otto, C., Reyer, C.P., Karger, D.N., Malle, J.T., *et al.*: Scenario setup and forcing data for impact model evaluation and impact attribution within the third round of the inter-sectoral impact model intercomparison project (isimip3a). *Geoscientific Model Development* **17**(1), 1–51 (2024)
- [44] Müller, C., Robertson, R.D.: Projecting future crop productivity for global economic modeling. *Agricultural Economics* **45**(1), 37–50 (2014)
- [45] Müller, C., Elliott, J., Chryssanthacopoulos, J., Arneth, A., Balkovic, J., Ciais, P., Deryng, D., Folberth, C., Glotter, M., Hoek, S., *et al.*: Global gridded crop model evaluation: benchmarking, skills, deficiencies and implications. *Geoscientific Model Development* **10**(4), 1403–1422 (2017)
- [46] Jägermeyr, J., Pastor, A., Biemans, H., Gerten, D.: Reconciling irrigated food production with environmental flows for sustainable development goals implementation. *Nature communications* **8**(1), 15900 (2017)
- [47] Schaphoff, S., Forkel, M., Müller, C., Knauer, J., Von Bloh, W., Gerten, D., Jägermeyr, J., Lucht, W., Rammig, A., Thonicke, K., *et al.*: Lpjml4—a dynamic global vegetation model with managed land—part 2: Model evaluation. *Geoscientific Model Development* **11**(4), 1377–1403 (2018)
- [48] Ronchetti, G., Nisini Scacchiafichi, L., Seguini, L., Cerrani, I., Velde, M.: Harmonized european union subnational crop statistics can reveal climate impacts and crop cultivation shifts. *Earth System Science Data* **16**(3), 1623–1649 (2024)
- [49] Lobell, D.B., Deines, J.M., Tommaso, S.D.: Changes in the drought sensitivity of us maize yields. *Nature Food* **1**(11), 729–735 (2020)
- [50] Vicente-Serrano, S.M., Beguería, S., López-Moreno, J.I.: A multiscalar drought index sensitive to global warming: the standardized precipitation evapotranspiration index. *Journal of climate* **23**(7), 1696–1718 (2010)
- [51] Nóia Júnior, R.d.S., Deswarte, J.-C., Cohan, J.-P., Martre, P., Der Velde, M., Lecerf, R., Webber, H., Ewert, F., Ruane, A.C., Slafer, G.A., *et al.*: The extreme 2016 wheat yield failure in france. *Global Change Biology* **29**(11), 3130–3146 (2023)
- [52] Zipper, S.C., Qiu, J., Kucharik, C.J.: Drought effects on us maize and soybean production: spatiotemporal patterns and historical changes. *Environmental Research Letters* **11**(9), 094021 (2016)
- [53] Deines, J.M., Archontoulis, S.V., Huber, I., Lobell, D.B.: Observational evidence for groundwater influence on crop yields in the united states. *Proceedings of the National Academy of Sciences* **121**(36), 2400085121 (2024)

- [54] Frieler, K., Schauburger, B., Arneth, A., Balkovič, J., Chryssanthacopoulos, J., Deryng, D., Elliott, J., Folberth, C., Khabarov, N., Müller, C., *et al.*: Understanding the weather signal in national crop-yield variability. *Earth's Future* **5**(6), 605–616 (2017)
- [55] Garcia-Vila, M., Santos Vianna, M., Harrison, M.T., Liu, K., S. Nóia-Júnior, R., Weber, T.K., Zhao, J., Acutis, M., Archontoulis, S., Asseng, S., *et al.*: Gaps and strategies for accurate simulation of waterlogging impacts on crop productivity. *Nature Food*, 1–10 (2025)
- [56] Proctor, J., Zeppetello, L.V., Chan, D., Huybers, P.: Climate change increases the interannual variance of summer crop yields globally through changes in temperature and water supply. *Science Advances* **11**(36), 3575 (2025)
- [57] Heinicke, S., Frieler, K., Jägermeyr, J., Mengel, M.: Global gridded crop models underestimate yield responses to droughts and heatwaves. *Environmental Research Letters* **17**(4), 044026 (2022)
- [58] Nóia Júnior, R.d.S., Asseng, S., Müller, C., Deswarte, J.-C., Cohan, J.-P., Martre, P.: Negative impacts of climate change on crop yields are underestimated. *Trends Plant Sci.* **30**(11), 1262–1273 (2025) <https://doi.org/10.1016/j.tplants.2025.05.002>
- [59] Ben-Ari, T., Boé, J., Ciais, P., Lecerf, R., Velde, M., Makowski, D.: Causes and implications of the unforeseen 2016 extreme yield loss in the breadbasket of france. *Nature communications* **9**(1), 1627 (2018)
- [60] Pastorello, G., Trotta, C., Canfora, E., Chu, H., Christianson, D., Cheah, Y.-W., Poindexter, C., Chen, J., Elbashandy, A., Humphrey, M., *et al.*: The fluxnet2015 dataset and the oneflux processing pipeline for eddy covariance data. *Scientific data* **7**(1), 225 (2020)
- [61] Chu, H., Christianson, D.S., Cheah, Y.-W., Pastorello, G., O'Brien, F., Geden, J., Ngo, S.-T., Hollowgrass, R., Leibowitz, K., Beekwilder, N.F., *et al.*: Ameriflux base data pipeline to support network growth and data sharing. *Scientific Data* **10**(1), 614 (2023)
- [62] Gelbrecht, M., Klöwer, M., Boers, N.: Pseudospectralnet: Toward hybrid atmospheric models for climate simulations. *Journal of Advances in Modeling Earth Systems* **17**(10), 2025–004969 (2025)
- [63] Chen, R.T., Rubanova, Y., Bettencourt, J., Duvenaud, D.K.: Neural ordinary differential equations. *Advances in neural information processing systems* **31** (2018)
- [64] Bezanson, J., Edelman, A., Karpinski, S., Shah, V.B.: Julia: A fresh approach to numerical computing. *SIAM review* **59**(1), 65–98 (2017)

- [65] Innes, M.: Don't unroll adjoint: Differentiating ssa-form programs. CoRR **abs/1810.07951** (2018) [arXiv:1810.07951](https://arxiv.org/abs/1810.07951)
- [66] Mialyk, O., Schyns, J.F., Booiij, M.J., Su, H., Hogeboom, R.J., Berger, M.: Water footprints and crop water use of 175 individual crops for 1990–2019 simulated with a global crop model. *Scientific data* **11**(1), 206 (2024)
- [67] Okada, M., Iizumi, T., Sakurai, G., Hanasaki, N., Sakai, T., Okamoto, K., Yokozawa, M.: Modeling irrigation-based climate change adaptation in agriculture: Model development and evaluation in northeast china. *Journal of Advances in Modeling Earth Systems* **7**(3), 1409–1424 (2015)
- [68] Balkovič, J., Velde, M., Skalský, R., Xiong, W., Folberth, C., Khabarov, N., Smirnov, A., Mueller, N.D., Obersteiner, M.: Global wheat production potentials and management flexibility under the representative concentration pathways. *Global and Planetary Change* **122**, 107–121 (2014)
- [69] Song, Y., Jain, A., McIsaac, G.: Implementation of dynamic crop growth processes into a land surface model: evaluation of energy, water and carbon fluxes under corn and soybean rotation. *Biogeosciences* **10**(12), 8039–8066 (2013)
- [70] Haas, E., Klatt, S., Fröhlich, A., Kraft, P., Werner, C., Kiese, R., Grote, R., Breuer, L., Butterbach-Bahl, K.: Landscapedndc: a process model for simulation of biosphere–atmosphere–hydrosphere exchange processes at site and regional scale. *Landscape ecology* **28**(4), 615–636 (2013)
- [71] Ma, J., Olin, S., Anthoni, P., Rabin, S.S., Bayer, A.D., Nyawira, S.S., Arneeth, A.: Modeling symbiotic biological nitrogen fixation in grain legumes globally with lpj-guess (v4. 0, r10285). *Geoscientific Model Development* **15**(2), 815–839 (2022)
- [72] Williams, J., Jones, C., Kiniry, J., Spanel, D.A.: The epic crop growth model. *Transactions of the ASAE* **32**(2), 497–0511 (1989)
- [73] Jones, J.W., Hoogenboom, G., Porter, C.H., Boote, K.J., Batchelor, W.D., Hunt, L.A., Wilkens, P.W., Singh, U., Gijsman, A.J., Ritchie, J.T.: The dssat cropping system model. *European journal of agronomy* **18**(3-4), 235–265 (2003)
- [74] Enders, A., Vianna, M., Gaiser, T., Krauss, G., Webber, H., Srivastava, A.K., Seidel, S.J., Tewes, A., Rezaei, E.E., Ewert, F.: Simplace—a versatile modelling and simulation framework for sustainable crops and agroecosystems. *in silico Plants* **5**(1), 006 (2023)
- [75] Hurtt, G.C., Chini, L., Sahajpal, R., Frohking, S., Bodirsky, B.L., Calvin, K., Doelman, J.C., Fisk, J., Fujimori, S., Goldewijk, K.K., *et al.*: Harmonization of global land-use change and management for the period 850–2100 (luh2) for cmip6. *Geoscientific Model Development Discussions* **2020**, 1–65 (2020)

- [76] Dietrich, J.P., Mishra, A., Weindl, I., Boudirsky, B.L., Wang, X., Baumstark, L., Kreidenweis, U., Klein, D., Steinmetz, N., Chen, D., Humpenoeder, F., von Jeetze, P., Wirth, S., Beier, F., Hoetten, D., Sauer, P., Tommey, J.: mrland: MadRaT land data package. Version: 0.65.11 (2025). <https://doi.org/10.5281/zenodo.3822083> . <https://github.com/pik-piam/mrland>
- [77] Porwolik, V., Rolinski, S., Heinke, J., Müller, C.: Generating a rule-based global gridded tillage dataset. *Earth System Science Data* **11**(2), 823–843 (2019)

## Extended Data Figures

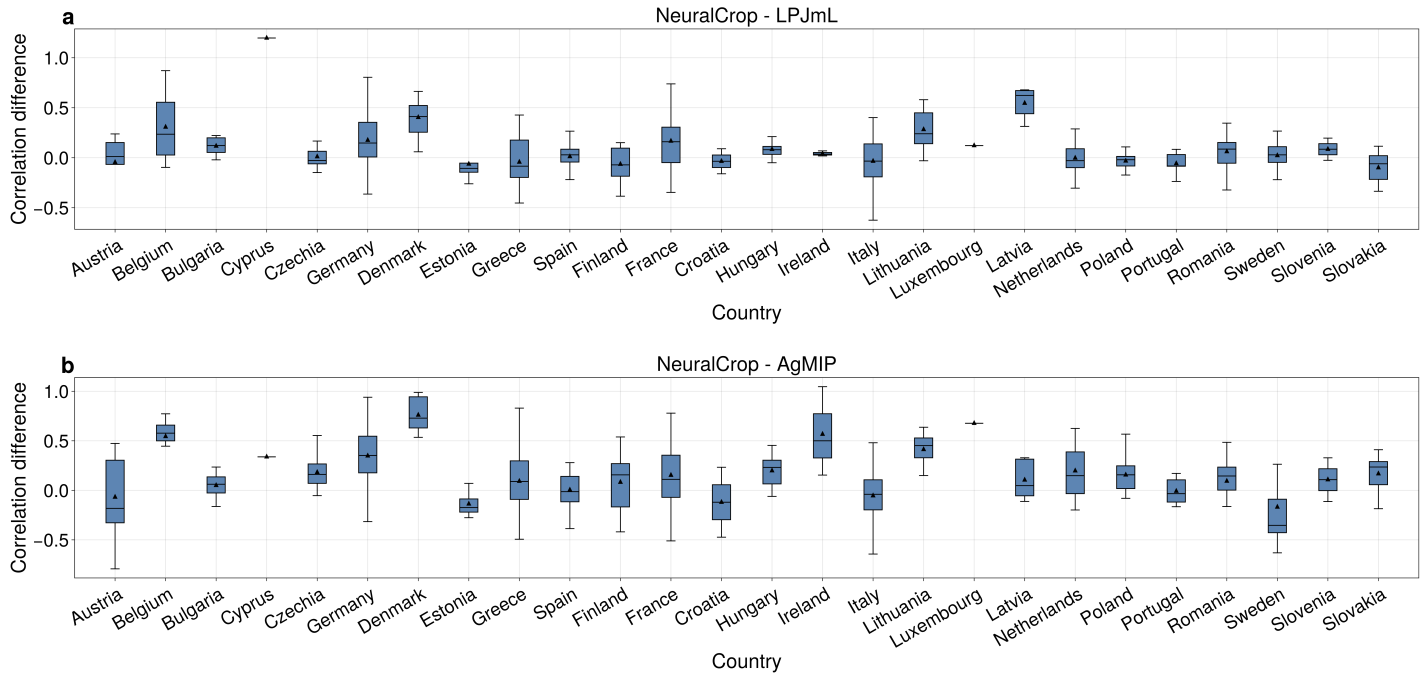


**Fig. 6** Correlation coefficient difference between NeuralCrop and GGCMs in European wheat regions. **a**, Boxplots of the correlation coefficient difference between NeuralCrop and LPJmL at the subnational level, aggregated by country for the period 2000–2016, with countries ordered alphabetically by their country code (A–Z). The box boundaries represent the interquartile range (IQR), defined by the first quartile, the median, and the third quartile. The upper and lower whiskers represent the maximum and minimum values that are within 1.5 times the interquartile range of the box. The black triangles are the mean values. NeuralCrop outperforms (underperforms) LPJmL in 16 (10) of the 26 countries. **b**, Same as panel a but for the correlation coefficient difference between NeuralCrop and AgMIP (the ensemble median of 8 GGCMs). NeuralCrop outperforms (underperforms) LPJmL in 19 (7) of the 26 countries.

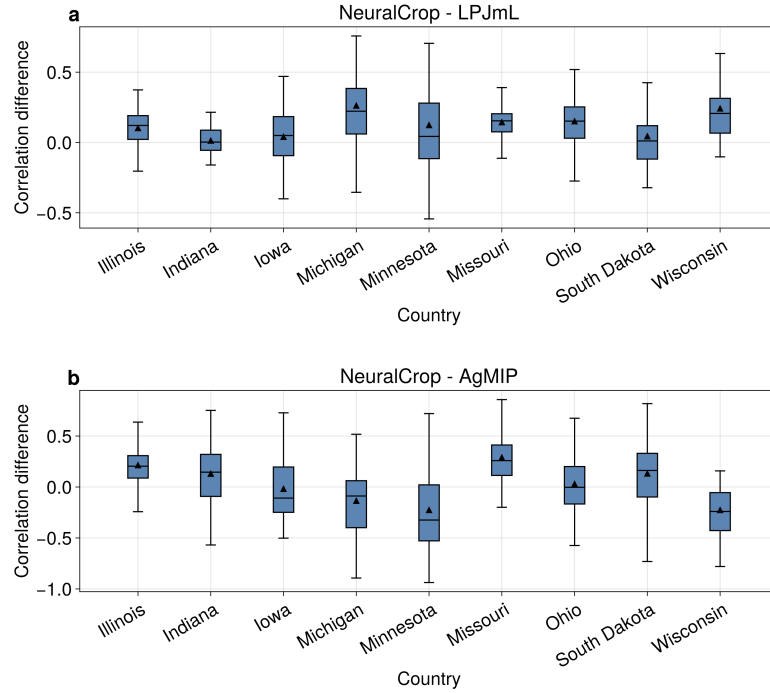


**Fig. 7** Correlation coefficient difference between NeuralCrop and GGCMs in the US Corn Belt, including nine states (i.e., South Dakota, Minnesota, Iowa, Missouri, Wisconsin, Illinois, Michigan, Indiana, and Ohio). **a**, Boxplots of the correlation coefficient difference between NeuralCrop and LPJmL at the county level, aggregated by state for the period 2000–2016. The box boundaries represent the interquartile range (IQR), defined by the first quartile, the median, and the third quartile. The upper and lower whiskers represent the maximum and minimum values that are within 1.5 times the interquartile range of the box. The black triangles are the mean values. NeuralCrop outperforms (underperforms) LPJmL in 7 (2) of the 9 states. **b**, Same as panel a but for the correlation coefficient difference between NeuralCrop and AgMIP (the ensemble median of 8 GGCMs). NeuralCrop outperforms (underperforms) LPJmL in 4 (5) of the 9 states.

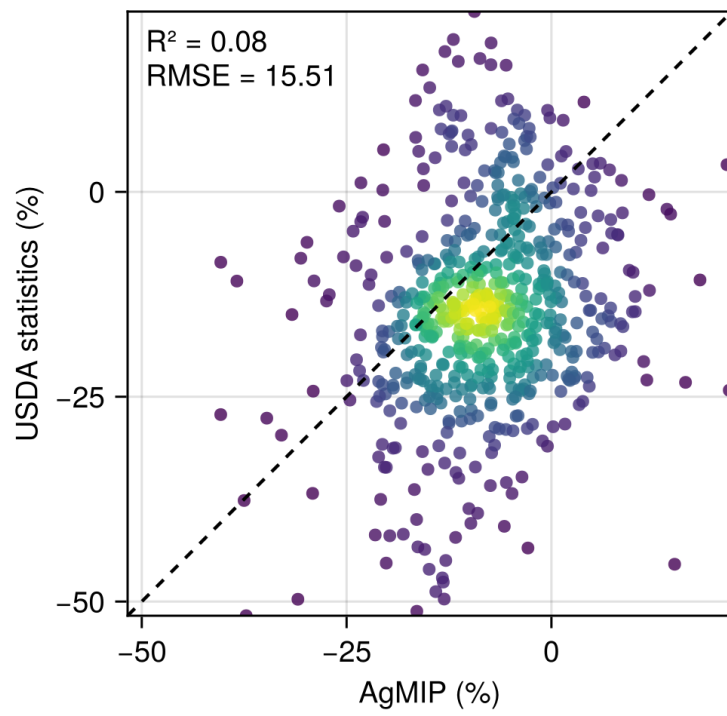


**Fig. 8** Simulated corn yield anomalies (%) by AgMIP (the ensemble median of 8 GGCMs) against USDA statistics (benchmark). The color gradient indicates the density of data points, and the dashed line represents the 1:1 line.  $R^2$  and RMSE values are shown in the upper left.

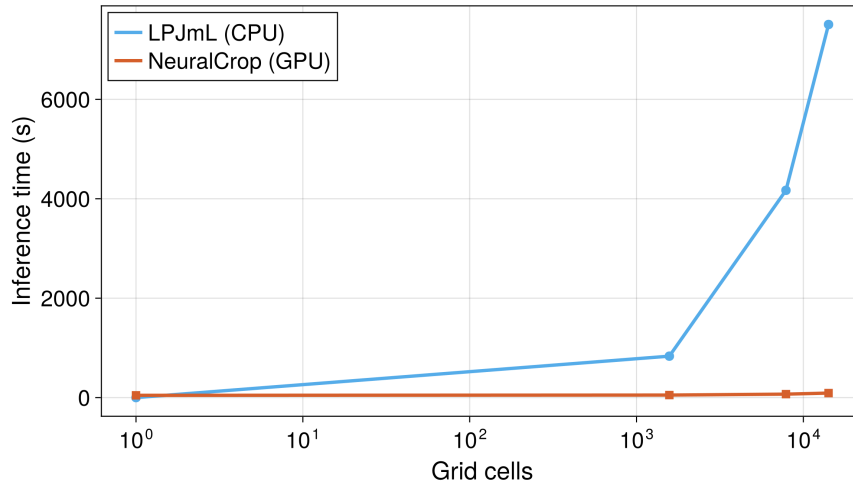


**Fig. 9** Inference time of GPU-accelerated NeuralCrop and CPU-based LPJmL simulating for a  $0.5^\circ \times 0.5^\circ$  spatial resolution with daily time steps over a 20-year simulation period (7300 days) at different grid cells. NeuralCrop was running on one single NVIDIA H100 GPU with 80GB of memory, and LPJmL was running on one single AMD EPYC 9554 CPU with 128 cores and 768GB of memory.

# Supplementary information

<b>A Hybrid architecture</b>	<b>31</b>
A.1 Dynamical Core of NeuralCrop	31
A.2 Neural network	31
A.3 Implementation	31
<b>B Trainable components of NeuralCrop</b>	<b>33</b>
B.1 Photosynthesis	33
B.2 Crop carbon allocation	35
B.3 Soil and litter carbon cycle	36
B.4 Soil and litter nitrogen cycle	37
B.5 Soil water cycle	38
<b>C Data</b>	<b>40</b>
C.1 Initial conditions	40
C.2 Pre-training data	40
C.3 Fine-tuning data	40
C.4 Data pre-processing	41
<b>D Training</b>	<b>43</b>
D.1 Input data normalization	43
D.2 Optimizer settings	43
D.3 Loss function	43
D.4 Training sequence length	44
D.5 Training rollouts	44
D.6 Output rescaling	46
D.7 Training resources	46
<b>E Evaluation metrics</b>	<b>47</b>
E.1 Pearson correlation coefficient	47
E.2 Coefficient of determination	47
E.3 Root mean square error	47
<b>F In situ validation</b>	<b>48</b>
F.1 In situ sites	48
F.2 Training	48
F.3 Results	49
<b>G Large-scale cropping regions</b>	<b>55</b>
G.1 European wheat	55
G.1.1 Subnational crop statistics	55
G.1.2 Pre-training	55
G.1.3 Fine-tuning	56
G.2 US Corn Belt	57

G.2.1	County-level crop statistics	57
G.2.2	Pre-training	58
G.2.3	Fine-tuning	59
G.3	Out-of-sample generalization	60
G.4	SPEI	62
<b>H</b>	<b>Yield data processing</b>	<b>64</b>
H.1	Yield aggregation	64
H.2	Yield detrending	64
H.3	Yield anomalies	65
<b>I</b>	<b>Additional information</b>	<b>66</b>
I.1	Case study	66
I.2	France wheat anomalies in 2016	68

## A Hybrid architecture

### A.1 Dynamical Core of NeuralCrop

NeuralCrop distinguishes between diagnostic and prognostic variables. Diagnostic variables, such as leaf area index (LAI) and gross primary productivity (GPP), represent instantaneous system states that are not explicitly dependent on the system’s temporal evolution. Prognostic variables, such as carbon pools, nitrogen pools and soil water pools, govern the dynamic evolution of the system states over time. They are represented by coupled ordinary differential equations (ODEs) that form the dynamical core of NeuralCrop in crop carbon, nitrogen, and water cycles, as described in detail in Section B. At each time step, diagnostic variables are updated based on the computed prognostic variables.

### A.2 Neural network

In NeuralCrop, we combine fully-connected neural networks with process-based components, which are designed to learn key process representations from observational data, to reduce ‘hidden’ uncertainties inherent in process-based GGCMs. For diagnostic variables replaced or augmented by neural networks, we use a 5-layer MLP with ReLU activations and 384 hidden neurons. To capture temporal dependencies and continuous dynamics, we naturally use neural ordinary differential equations (NODEs) [1] to model prognostic variables, which are parameterized by a 3-layer MLP with ReLU activations and 384 hidden neurons. To solve the NODEs, we use a forward Euler solver with a fixed time step  $\Delta t = 1$  day. At each time step  $t$ , the prognostic variable  $\mathbf{X}(t)$  is updated according to:

$$\mathbf{X}(t + \Delta t) = \mathbf{X}(t) + \Delta t \cdot f_{\theta}(\mathbf{X}(t), t) \quad (\text{S1})$$

where  $f_{\theta}$  denotes the MLP that outputs the learned tendencies.

### A.3 Implementation

NeuralCrop adopts robust physical representations of ecosystem processes governing carbon, water, energy, and nitrogen fluxes from LPJmL, a state-of-the-art process-based model in simulating natural and agricultural ecosystems. To enable seamless integration with machine learning components, we translated the C-based crop module of LPJmL into Julia, a high-performance language designed for numerical and scientific computing [2]. The Julia ecosystem for scientific machine learning (SciML) provides native support for differential equations [3], which naturally fits well with our hybrid modelling approach using ODEs as the core of system dynamics.

We implement the ML components of NeuralCrop using Lux.jl [4, 5], a neural network framework built entirely with pure functions that are friendly to both compilers and automatic differentiation. We train the ML components of NeuralCrop using Zygote.jl [6], a high-performance automatic differentiation (AD) framework in Julia that enables efficient gradient-based optimization, accelerated by CUDA.jl [7, 8]. During training, the gradients of neural networks are computed via direct reverse-mode

differentiation, including the forward Euler solver used for the NODEs (i.e., gradients are obtained by backpropagating through the Euler solver rather than using adjoint methods). To support full graphics-processing-unit (GPU) compatibility and improve computational efficiency, we implement the process-based components using KernelAbstractions.jl [9], which allows both neural networks and process-based parts to be parallelized and executed within a unified GPU-accelerated framework.



where  $C_2$  is the stomatal conductance-related coefficient, and  $V_{\max}$  is the maximum Rubisco capacity.

$$A_{\text{gd}} = \frac{\left( J_{\text{E}} + J_{\text{C}} - \sqrt{(J_{\text{E}} + J_{\text{C}})^2 - 4 \cdot \theta \cdot J_{\text{E}} \cdot J_{\text{C}}} \right)}{2 \cdot \theta \cdot \text{daylength}}, \quad (\text{S4})$$

where  $\theta$  is the co-limitation coefficient of light and Rubisco activity.

Here, we only present the final equation to obtain  $A_{\text{gd}}$  (Eq. S4) and omit the intermediate derivation steps, which are already described in detail in Schaphoff et al.[10]. In order to compute the optimal ratio of the inter-cellular to atmospheric  $\text{CO}_2$  concentration,  $\lambda$ , the following equation must be solved (Eq. S5).

$$A_{\text{nd}} + (1 - \text{daylength}/24) \cdot R_{\text{leaf}} - p_{\text{a}} \cdot (g_{\text{c}} - g_{\text{min}}) \cdot (1 - \lambda)/1.6 = 0, \quad (\text{S5})$$

where  $A_{\text{nd}}$  is daily net photosynthesis rate,  $R_{\text{leaf}}$  is leaf respiration,  $p_{\text{a}}$  is the atmospheric partial pressure of  $\text{CO}_2$ ,  $g_{\text{c}}$  is canopy conductance,  $g_{\text{min}}$  is vegetation (crop) specific minimum canopy conductance. However, an analytical solution is not feasible because  $\lambda$  appears both directly in the equation and indirectly through  $A_{\text{nd}}$ . In LPJmL, a bisection algorithm is used to iteratively solve the equation and determine the value of  $\lambda$ , which introduces high computational cost when conducting large-scale, high-resolution simulations.

To address this bottleneck, we replace the root-finding algorithm with a 5-layer MLP to emulate the solution for  $\lambda$ , which approximates the nonlinear relationship between environmental variables (i.e., day length, air temperature, and soil moisture) and the corresponding optimal value of  $\lambda$ . Compared to the bisection algorithm, the neural network-based emulator can significantly accelerate the photosynthesis computation, which is due to the fact that neural networks only need one forward pass for inference, while root-finding algorithms involve iterative evaluations.

Additionally, we use a second 5-layer MLP to simulate the maximum Rubisco capacity  $V_{\max}$ , originally computed using an empirical formulation (Eq. S6).

$$V_{\max} = (N_{\text{leaf}} - NC_{\text{leaf, low}} \cdot C_{\text{leaf}}) / (p \cdot \exp(k_{\text{temp}} \cdot (T - 25)) \cdot \text{LAI}) \cdot \text{daylength} \quad (\text{S6})$$

where  $N_{\text{leaf}}$  is the leaf nitrogen content,  $C_{\text{leaf}}$  is the leaf carbon content,  $NC_{\text{leaf, low}}$  is the crop-specific lower ratio of leaf carbon and nitrogen,  $p$  is the static coefficient,  $k_{\text{temp}}$  is the factor of temperature dependence of nitrogen demand for Rubisco activity,  $T$  is the air temperature, LAI is the leaf area index. Instead of relying on a fixed empirical relationship, this neural network is trained using observational data to capture more complex and potentially nonlinear interactions between  $V_{\max}$  and its environmental and biochemical drivers (i.e., day length, APAR, leaf nitrogen, and air temperature).

Furthermore, we implement the photosynthesis module to be fully differentiable. By leveraging observational GPP, we are able to optimize  $\lambda$  and  $V_{\max}$  through gradient-based 'online training', which helps mitigate "hidden" biases introduced by the original empirical formulation of  $\lambda$  and  $V_{\max}$ .

## B.2 Crop carbon allocation

In LPJmL, crop carbon allocation is governed by a set of heuristic rules driven by phenological development stage, organ priority, and stress factors. Daily NPP (net gross productivity) accumulates to total biomass, which is then allocated to crop organs in a hierarchical order: root, leaf, storage organ, mobile reserve, and stem [10]. The carbon allocation equations are:

$$C_{\text{root}} = f_{\text{root}} \cdot \text{biomass}, \quad (\text{S7})$$

$$C_{\text{leaf}} = \frac{\text{LAI}}{\text{sla}}, \quad (\text{S8})$$

$$C_{\text{so}} = \text{HI} \cdot (1 - f_{\text{root}}) \cdot \text{biomass}, \quad (\text{S9})$$

$$C_{\text{pool}} = \text{biomass} - C_{\text{root}} - C_{\text{leaf}} - C_{\text{so}}. \quad (\text{S10})$$

where  $f_{\text{root}}$  is the root carbon allocation coefficient (co-limited by water and nitrogen stress),  $\text{sla}$  is the specific leaf area, HI is the harvest index (limited by water stress). The daily carbon allocation is computed based solely on the current phenological and environmental conditions without tracking the dynamic evolution of carbon pools over time, which limits its ability to represent feedbacks and lagged responses.

The matrix-based carbon allocation framework proposed by Luo et al. [17] provides a promising approach to model carbon allocation dynamics. By representing carbon allocation as a system of ODEs (Eq. S11), it captures the temporal evolution of carbon pools in a continuous and prognostic manner.

$$\frac{dC(t)}{dt} = A(C, t)\mu(t) + B(C, t)\xi(t)K(C, t)C(t), \quad (\text{S11})$$

where  $C(t)$  denotes the vector of carbon compartments,  $A(C, t)$  is a vector of allocation coefficients,  $\mu(t)$  is carbon input (e.g., NPP),  $B(C, t)$  is a matrix of transfer coefficients,  $\xi(t)$  is a matrix of environmental modifiers,  $K(C, t)$  is a matrix of turnover coefficients. Despite its advantages, a key challenge of the matrix-based formulation is the parameterization of the matrices  $A$ ,  $B$ , and  $K$ , which requires detailed mechanistic assumptions or extensive calibration. Such parameterizations are often poorly constrained and exhibit high spatial heterogeneity, making it difficult to apply the model robustly under diverse environmental and management conditions.

Here, we further extend the matrix approach using neural ordinary differential equations (NODEs), where the right-hand side of ODEs is replaced by neural networks [1]. Specifically, we use a 3-layer MLP to parameterize the carbon allocation dynamics (the right-hand side of Eq. S11) implicitly based on carbon pool states and external inputs (i.e., NPP, LAI, leaf nitrogen, and soil moisture). This NODE-based formulation avoids explicitly prescribing the allocation, transfer, and turnover coefficients while introducing data-driven flexibility to better capture the complexity and variability of crop-environment interactions. Our choice of matrix approach was also motivated by our desire for efficient running on machine learning accelerators, in particular GPUs, which are highly optimized for matrix operations.

### B.3 Soil and litter carbon cycle

Agricultural soil and litter carbon play a crucial role in the global carbon balance under climate change. In LPJmL, the litter carbon consists of three litter pools, including two above-ground leaf and stem litter carbon pools and one below-ground root litter carbon pool. The soil carbon is simulated across five vertical soil layers (0.2, 0.3, 0.5, 1, and 1 meter thickness) with a fast and a slow organic carbon pool in each layer [18]. LPJmL uses discrete-time balance equations to update each soil and litter carbon pool. Based on the matrix approach, we reformulated the soil and litter carbon balance as explicit ODEs (Eqs. S12 - S14), which are well suited for parallel execution on GPUs.

$$\frac{dC_{\text{litter}}(t, l)}{dt} = A_{\text{litter}} \cdot C_{\text{residue}} - (1 - \exp(-k_{\text{litter}10} \cdot f_{\text{litter}}(t, l))) \cdot C_{\text{litter}}(t, l), \quad (\text{S12})$$

with  $l = 1, 2, 3$ ,

where  $C_{\text{residue}}$  denotes the crop residues after crops are harvested,  $A_{\text{litter}}$  is the crop residue partitioning coefficients,  $k_{\text{litter}10}$  is the static litter carbon decomposition rate at 10 °C,  $f_{\text{litter}}(t, l)$  is the carbon decomposition response function. Above-ground litter carbon decomposition depends on air temperature and soil moisture, whereas below-ground litter carbon decomposition depends on soil temperature and soil moisture. The second term of Eq. S12 is the daily decomposed litter carbon, at which 70% of decomposed litter carbon directly enters the atmosphere as litter respiration, and the remaining goes into the soil carbon pools, with 98.5% to the fast soil carbon pools and 1.5% to the slow carbon pools [18].

$$\frac{dC_{\text{fast}}(t, l)}{dt} = A_{\text{fast}}\mu(t) - (1 - \exp(-k_{\text{fast}10} \cdot f_{\text{fast}}(t, l))) \cdot C_{\text{fast}}(t, l), \quad (\text{S13})$$

$$\frac{dC_{\text{slow}}(t, l)}{dt} = A_{\text{slow}}\mu(t) - (1 - \exp(-k_{\text{slow}10} \cdot f_{\text{slow}}(t, l))) \cdot C_{\text{slow}}(t, l), \quad (\text{S14})$$

with  $l = 1, 2, 3, 4, 5$ ,

where  $\mu(t)$  is the carbon input from decomposed litter carbon,  $A_{\text{fast}}$  and  $A_{\text{slow}}$  are the carbon input partitioning coefficients across five layers,  $k_{\text{fast}0}$  and  $k_{\text{slow}0}$  are the static soil carbon decomposition rate at 10 °C,  $f_{\text{fast}}(t, l)$  and  $f_{\text{slow}}(t, l)$  are the carbon decomposition response functions which depends on soil temperature and soil moisture. Both the second term of Eq. S13 and Eq. S14 are the daily decomposed soil carbon, which directly goes into the atmosphere as soil respiration.

The original formulation of the response function is a cubic polynomial equation:

$$f = \exp \left[ 308.56 \cdot \left( \frac{1}{56.02} - \frac{1}{T + 46.02} \right) \right] \cdot (0.0402 - 5.005 \cdot \theta^3 + 4.269 \cdot \theta^2 + 0.719 \cdot \theta), \quad (\text{S15})$$

where  $(T)$  denotes air or soil temperature,  $\theta$  is soil moisture. We replace the decomposition response functions  $f_{\text{litter}}(t, l)$ ,  $f_{\text{fast}}(t, l)$ , and  $f_{\text{slow}}(t, l)$  in Eqs. S12 - S14 with a

3-layer MLP that takes both soil temperature and soil moisture as inputs, respectively. This allows the model to flexibly capture nonlinear environmental effects in a fully data-driven manner, rather than relying on fixed cubic polynomial response functions.

## B.4 Soil and litter nitrogen cycle

In LPJmL, the soil and litter nitrogen cycle is tightly coupled to the soil and litter carbon cycle and follows a structurally similar formulation, including three litter nitrogen pools and a fast and a slow nitrogen pool in each soil layer [19]. We also reformulated the soil and litter nitrogen balance as explicit ODEs (Eqs. S16-S18).

$$\frac{dN_{\text{litter}}(t, l)}{dt} = A_{\text{litter}} \cdot N_{\text{residue}} - (1 - \exp(-k_{\text{litter}10} \cdot f_{\text{litter}}(t, l))) \cdot N_{\text{litter}}(t, l), \quad (\text{S16})$$

with  $l = 1, 2, 3$ ,

where  $N_{\text{residue}}$  denotes the crop residues after crops are harvested,  $A_{\text{litter}}$  is the crop residue partitioning coefficients,  $k_{\text{litter}10}$  is the static litter nitrogen decomposition rate at 10 °C,  $f_{\text{litter}}(t, l)$  is the nitrogen decomposition response function. Above-ground litter nitrogen decomposition depends on air temperature and soil moisture, whereas below-ground litter nitrogen decomposition depends on soil temperature and soil moisture. The second term of Eq. S16 is the daily decomposed litter nitrogen, at which 70% of decomposed litter nitrogen directly enters the atmosphere as litter respiration, and the remaining goes into the soil nitrogen pools, with 98.5% to the fast soil nitrogen pools and 1.5% to the slow nitrogen pools [18].

$$\frac{dN_{\text{fast}}(t, l)}{dt} = A_{\text{fast}}\mu(t) - (1 - \exp(-k_{\text{fast}10} \cdot f_{\text{fast}}(t, l))) \cdot N_{\text{fast}}(t, l), \quad (\text{S17})$$

$$\frac{dN_{\text{slow}}(t, l)}{dt} = A_{\text{slow}}\mu(t) - (1 - \exp(-k_{\text{slow}10} \cdot f_{\text{slow}}(t, l))) \cdot N_{\text{slow}}(t, l), \quad (\text{S18})$$

with  $l = 1, 2, 3, 4, 5$ ,

where  $\mu(t)$  is the nitrogen input from decomposed litter nitrogen,  $A_{\text{fast}}$  and  $A_{\text{slow}}$  are the nitrogen input partitioning coefficients across five layers,  $k_{\text{fast}0}$  and  $k_{\text{slow}0}$  are the static soil nitrogen decomposition rate at 10 °C,  $f_{\text{fast}}(t, l)$  and  $f_{\text{slow}}(t, l)$  are the nitrogen decomposition response functions which depends on soil temperature and soil moisture. Both the second term of Eq. S17 and Eq. S18 are the daily decomposed soil nitrogen, which directly goes into the atmosphere as soil respiration.

The original formulation of the response function follows Eq. S15. We replace the decomposition response functions  $f_{\text{litter}}(t, l)$ ,  $f_{\text{fast}}(t, l)$ , and  $f_{\text{slow}}(t, l)$  in Eqs. S16 - S18 with a 3-layer MLP that takes both soil temperature and soil moisture as inputs, respectively. This allows the model to flexibly capture nonlinear environmental effects in a fully data-driven manner, rather than relying on fixed cubic polynomial response functions.

## B.5 Soil water cycle

Similar to soil carbon and nitrogen, soil water in LPJmL is represented by five hydrologically active layers. Rather than explicitly solving the governing partial differential equations [10, 20], LPJmL simulates daily soil-water dynamics with a computationally efficient bucket model as follows:

$$W_t = W_{t-1} + \Delta t [(P + M + Irr - E_I) - R - (E_S + E_T) - p], \quad (\text{S19})$$

where  $W$  is the absolute soil water content in a specific soil layer,  $P$  is the precipitation,  $M$  is the snowmelt,  $Irr$  is the irrigation water,  $E_I$  is the interception loss from leaves,  $R$  is the runoff,  $E_S$  is the soil evaporation,  $E_T$  is the plant transpiration, and  $p$  is the percolation. The  $\Delta t$  is the model time step, which is fixed to one day in LPJmL so that all flux terms are expressed as daily rates. LPJmL assumes that  $E_S$  occurs only in bare soil with vegetation cover less than 100% and that water required for evaporation is available from the top 0.3 meters of soil. The soil water accessible for  $E_T$  depends on the root depth of vegetation. The structure of Eq. S19 is inherently discrete but equivalent to an explicit first-order ODE for a fixed time step. We reformulated it as a first-order ODE (Eq. S20), which allows the use of differentiable ODE solvers, enabling efficient gradient-based optimization for ML models.

$$\frac{dW}{dt} = (P + M + Irr - E_I) - R - (E_S + E_T) - p. \quad (\text{S20})$$

Compared to the soil carbon cycle, the soil water cycle is inherently more complex, involving a broader range of interacting processes, which leads to significantly higher uncertainty in predictions. Although the ODE-based soil water representation (Eq. S20) is numerically tractable, it relies on empirical formulas and fixed parameters. Such simplifications limit its ability to capture the complex spatio-temporal nonlinear processes, especially under diverse land cover types, soil properties, and climatic conditions.

To address the above limitations of Eq. S20, we integrate neural networks with soil water processes to augment the traditional process-based formulation with data-driven flexibility. We could use neural networks to replace the entire right-hand side of Eq. S20 to get a fully data-driven soil water representation, or replace only specific sub-processes to get a hybrid model. To compare both approaches, we implement a 3-layer MLP to replace  $M$  and  $E_S$  leading to a hybrid model, and a 3-layer MLP to fully emulate the daily soil water dynamics, respectively. The reason to replace  $M$  and  $E_S$  was based purely on empirical evidence. Through extensive testing, we found that replacing these two sub-processes yielded the most stable long-term simulations, whereas replacing other or additional sub-processes often led to simulation instability due to weakened sub-process constraints. Moreover,  $M$  involves a complex heuristic snowmelt formulation, and using a neural network to emulate it can substantially reduce model complexity. These two models were trained using mean squared error as the training objective. Results indicate that the hybrid approach better captures the daily dynamics of soil water content both in-sample and out-of-sample scenarios than

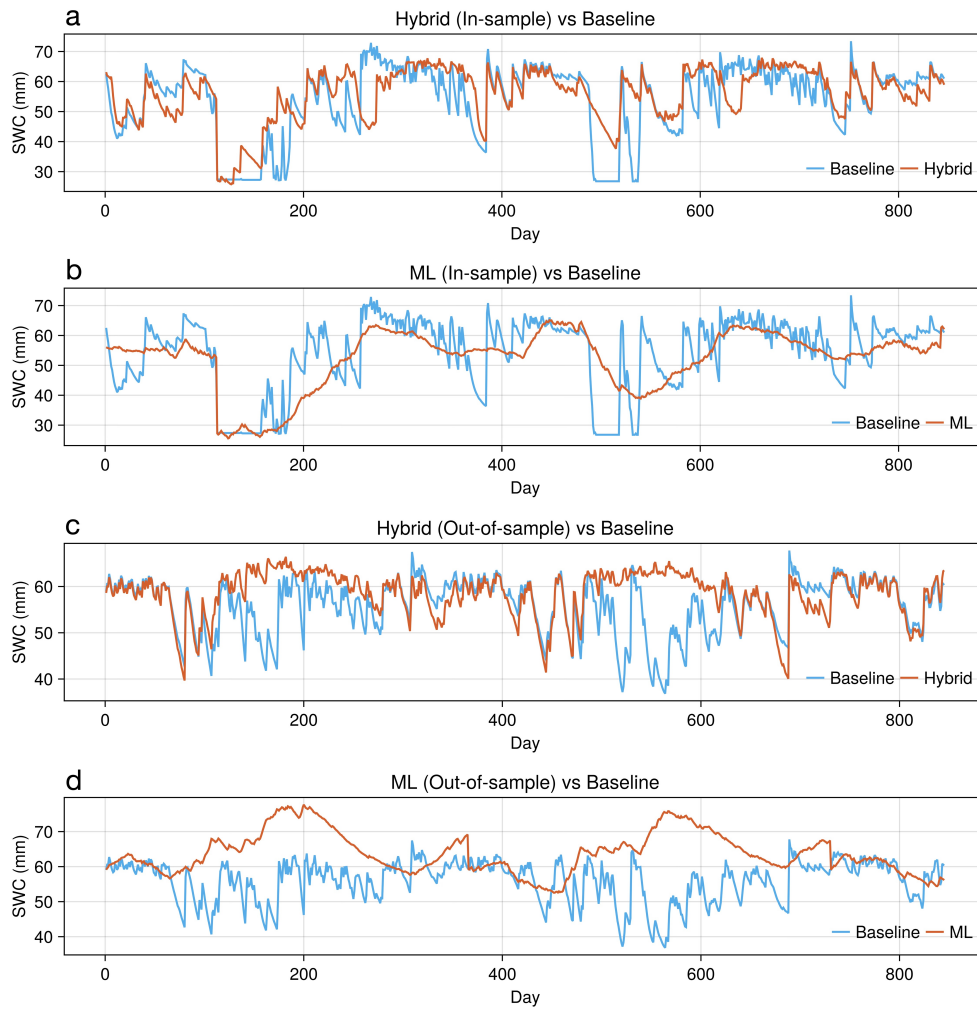


**Fig. S2** Comparison of soil water content (SWC) simulated by hybrid and pure machine learning models under in-sample and out-of-sample scenarios, with LPJmL-simulated SWC used as baseline. Panels a and b show in-sample performance for the hybrid and pure machine learning models, respectively, while panels c and d present their out-of-sample performance.

the fully data-driven alternative, as shown in Fig. S2. Due to the physical constraints of process-based components, the hybrid model more accurately captures rapid fluctuations in SWC and maintains consistency with the baseline across both in-sample and out-of-sample scenarios (Fig. S2, panels a and c), whereas the pure machine learning model exhibits overly smoothed responses and shows pronounced deviations from the baseline (Fig. S2, panels b and d), especially under out-of-sample scenarios. This indicates that incorporating process-based components with ML methods provides a more accurate and generalizable representation of soil hydrological processes.

## C Data

### C.1 Initial conditions

Before simulating managed croplands, process-based vegetation models usually need spin-up simulations to develop equilibrium vegetation and soil states. LPJmL involves a two-stage spin-up process. The first spin-up simulation typically runs for 5000 years until all system states (i.e., soil carbon, nitrogen, and water pools) reach equilibrium. The second spin-up simulation typically spans 390 years to introduce the impacts of land-use change on these pools driven by historical human activities [21]. Since NeuralCrop does not simulate natural vegetation, it can not perform this spin-up procedure prior to crop simulations. We therefore perform the spin-up in LPJmL and initialize the soil carbon, nitrogen, and water pools in NeuralCrop from LPJmL simulations to ensure physically consistent initial conditions.

### C.2 Pre-training data

Due to the limited availability of large-scale high-resolution observations for cropland carbon, water, and nitrogen dynamics, NeuralCrop is pre-trained on simulation data (Table S1) generated by LPJmL. This pre-training step allows NeuralCrop to learn prior knowledge from LPJmL and provides a strong initialization for subsequent training under data-scarce conditions. The LPJmL inputs are shown in Table S2.

**Table S1** Training data generated by LPJmL.

Variable	Symbol	Dimension	Units	Time
Inter-cellular to atmospheric CO <sub>2</sub> ratio	$\lambda$	1	-	daily
Maximum Rubisco capacity	$V_{\max}$	1	$\text{g C m}^{-2}$	daily
Gross primary productivity	GPP	1	$\text{g C m}^{-2}$	daily
Crop carbon pools	$C_i$	4	$\text{g C m}^{-2}$	daily
Litter carbon pools	$C_{\text{litter}(1)}$	3	$\text{g C m}^{-2}$	daily
Soil fast carbon pools	$C_{\text{fast}(1)}$	5	$\text{g C m}^{-2}$	daily
Soil slow carbon pools	$C_{\text{slow}(1)}$	5	$\text{g C m}^{-2}$	daily
Litter nitrogen pools	$N_{\text{litter}(1)}$	3	$\text{g N m}^{-2}$	daily
Soil fast nitrogen pools	$N_{\text{fast}(1)}$	5	$\text{g N m}^{-2}$	daily
Soil slow nitrogen pools	$N_{\text{slow}(1)}$	5	$\text{g N m}^{-2}$	daily
Soil water pools	$W_{(1)}$	5	mm	daily

### C.3 Fine-tuning data

During the fine-tuning stage, the training of NeuralCrop is focused on optimizing the ML components with real-world observations. The fine-tuning data were obtained from the global flux network FLUXNET, the American flux network AmeriFlux, and the European Integrated Carbon Observation System (ICOS), which provide site-level daily crop and soil eddy covariance flux as well as meteorological forcing measurements. Table S3 shows the observational data used during the fine-tuning stage. After the

**Table S2** LPJmL inputs.

Type	Variable	Units	Time
Climate	Temperature	°C	daily
Climate	Maximum temperature	°C	daily
Climate	Minimum temperature	°C	daily
Climate	Precipitation	mm	daily
Climate	Net longwave radiation	W/m <sup>2</sup>	daily
Climate	Downward shortwave radiation	W/m <sup>2</sup>	daily
Climate	Wind speed	m min <sup>-1</sup>	daily
Climate	CO <sub>2</sub>	ppmv	annual
Soil	Soil texture	-	static
Soil	Soil PH	-	static
Management	Land use	-	annual
Management	Nitrogen fertilizer	g N m <sup>-2</sup>	annual
Management	Tillage	-	annual
Management	Residue on field	-	annual
Management	Sowing date	-	static
Management	Heat unit requirements	-	static
Coordinate	Land sea mask	°C	static

pre-training stage, NeuralCrop is able to reproduce the dynamics of LPJmL, but also inherits its structural and knowledge biases. To address that, we optimize the parameters of the relevant ML components of NeuralCrop using data from flux networks, while freezing the remaining ML components.

**Table S3** Flux network observational data.

Type	Variable	Symbol	Units	Time
Feature	Air temperature	TA <sub>F</sub>	°C	daily
Feature	Precipitation	P <sub>F</sub>	mm	daily
Feature	Downward shortwave radiation	SW <sub>IN_F</sub>	W/m <sup>2</sup>	daily
Feature	Downward longwave radiation	LW <sub>IN_F</sub>	W/m <sup>2</sup>	daily
Feature	Upward longwave radiation	LW <sub>OUT</sub>	W/m <sup>2</sup>	daily
Feature	CO <sub>2</sub>	CO <sub>2F_MDS</sub>	μmol mol <sup>-1</sup>	daily
Label	Gross primary productivity	GPP <sub>NT_VUT_REF</sub>	g C m <sup>-2</sup>	daily
Label	Ecosystem Respiration	RECO <sub>NT_VUT_REF</sub>	g C m <sup>-2</sup>	daily
Label	Soil water content,	SWC <sub>F_MDS-#</sub>	%	daily

# denotes soil depth index, higher values represent deeper layers (1 is the shallowest).

## C.4 Data pre-processing

The flux networks provide both daytime and nighttime partitioned GPP and RECO [22, 23]. The nighttime method estimates RECO by fitting a respiration-temperature function using nighttime data and derives GPP as the difference between modeled RECO and daytime net ecosystem exchange (NEE). Because photosynthesis is negligible at night, RECO is approximately equal to NEE. The daytime method

fits a light-response function to estimate GPP and a respiration-temperature function for RECO using daytime and nighttime data. As a result, both GPP and RECO are estimated by NEE, which introduces coupled uncertainties. Therefore, we use nighttime partitioned GPP and RECO for fine-tuning. The nighttime partitioned GPP and RECO may contain negative values. We replace negative GPP and RECO with their daytime counterparts to avoid introducing an additional bias during fine-tuning.

The soil water content across flux tower sites is not standardized in the number of soil layers and their depth, which poses a challenge for consistent model training. To address this, we converted the soil water distribution into the five-layer structure used in NeuralCrop by aggregating or interpolating soil water data based on depth-weighted proportions aligned with the relative thicknesses of the NeuralCrop soil layers.

## D Training

### D.1 Input data normalization

All input features are standardized before being joined together and passed to the neural networks. We normalize climate forcings distributed with zero mean and unit variance to improve training stability. Specifically, for each climate forcing variable  $x$ , we compute the standardized value  $\tilde{x}$  as:

$$\tilde{x} = \frac{x - \mu}{\sigma}, \quad (\text{S21})$$

where  $\mu$  is the mean and  $\sigma$  is the standard deviation computed from the 20-year historical climatology. For input features generated by NeuralCrop itself, we rescale them to the  $[0, 1]$  range using their physical upper and lower bounds. Here, for each state variable  $x$ , the normalized value  $\tilde{x}$  is computed as:

$$\tilde{x} = \frac{x - x_{\text{lower}}}{x_{\text{upper}} - x_{\text{lower}}}, \quad (\text{S22})$$

where  $x_{\text{lower}}$  and  $x_{\text{upper}}$  denote the physical lower and upper limits of the variable, respectively.

### D.2 Optimizer settings

All NeuralCrop models were pre-trained using the AdamW optimizer [24]. We used values  $\beta_1 = 0.9$ ,  $\beta_2 = 0.999$ , and  $\epsilon = 10^{-6}$  based on empirical evidence from prior experiments. The initial learning rate was set to  $1 \times 10^{-3}$ . A sinusoidal exponential decay scheme (SinExp) was employed to dynamically adjust the learning rate throughout training, oscillating between  $1 \times 10^{-3}$  and  $1 \times 10^{-5}$  with a decay factor of 0.975 and a cycle period of 20 epochs. The only exception to these hyperparameters in fine-tuning was that the initial learning rate was set to  $1 \times 10^{-4}$ . All models were trained for 100 epochs using batch sizes 32, 64, 128, 256. We empirically selected the configuration that produced the most stable decrease in validation loss over time.

### D.3 Loss function

All NeuralCrop models are trained in two stages (pre-training and fine-tuning) with different loss functions, where all loss terms are defined in the general form of mean squared error (MSE):

$$\text{MSE} = \frac{1}{T} \sum_{t=1}^T (\hat{y}_t - y_t)^2, \quad (\text{S23})$$

where  $\hat{y}_t$  is the model simulation at time  $t$ ,  $y_t$  is the corresponding observation, and  $T$  is the total number of time steps.

During the pre-training stage, we employed a combination of two loss types (i.e., accuracy and mass balance) to minimize two kinds of discrepancies between NeuralCrop and LPJmL outputs. The loss term of accuracy accounts for the distance between predictions and reference data, and the loss term of mass balance constrains the carbon conservation during crop carbon allocation. The pre-training loss function has two kinds of loss types:

$$\mathcal{L}_{\text{Pre-training}} = \sum_{i \in \mathcal{T}} \beta_{\text{accuracy},i} \mathcal{M}_{\text{Accuracy},i} + \beta_{\text{mass}} \mathcal{M}_{\text{MassBalance}}, \quad (\text{S24})$$

where  $\mathcal{T}$  denotes the set of loss terms of accuracy (i.e.,  $\lambda$ ,  $V_{\text{max}}$ , GPP, carbon and nitrogen pools, soil water pools),  $\mathcal{M}_{\text{Accuracy},i}$  is the MSE between NeuralCrop prediction and reference data of variable  $i$  with corresponding loss scales  $\beta_{\text{accuracy},i}$ ,  $\mathcal{M}_{\text{MassBalance}}$  is the MSE between the sum of crop carbon and accumulated above-ground biomass with a loss scale  $\beta_{\text{mass}}$ .

After the pre-training stage, NeuralCrop was further fine-tuned with real-world observational data (i.e., the eddy-covariance flux data) to reduce the gap between model outputs and ground truth. During this stage, we only updated the ML components that correspond to variables with available observations (C.3). Here is the loss function:

$$\mathcal{L}_{\text{Fine-tuning}} = \beta_{\text{gpp}} \mathcal{M}_{\text{GPP}} + \beta_{\text{reco}} \mathcal{M}_{\text{RECO}} + \beta_{\text{swc}} \mathcal{M}_{\text{SWC}}, \quad (\text{S25})$$

where  $\mathcal{M}_{\text{GPP}}$ ,  $\mathcal{M}_{\text{RECO}}$ , and  $\mathcal{M}_{\text{SWC}}$  denote the MSE on GPP, RECO, and SWC, scaled by  $\beta_{\text{gpp}}$ ,  $\beta_{\text{reco}}$ , and  $\beta_{\text{swc}}$ , respectively.

#### D.4 Training sequence length

To investigate the required length of time series data for effective training, we trained several NeuralCrop models with identical parameters using time series data ranging from 1 to 20 years in length. We find that two years of data were sufficient to train NeuralCrop effectively. We further investigated two training strategies. The first strategy used 80% of the time series samples from two years for training and the remaining 20% for validation. The second strategy used the time series samples from the first two years for training, with the third year for validation. We found that both strategies yielded comparable performance.

#### D.5 Training rollouts

To explore the benefits of training with different rollouts (i.e., how many simulation days to update ML parameters), we trained the NeuralCrop models with identical model parameters on rollouts of 1, 30, 60, 180, 365, and 720 days (Fig. S3). We find that NeuralCrop trained on longer rollouts leads to significantly more stable convergence during training. In contrast, NeuralCrop trained on shorter rollouts, especially 1 day, exhibits large oscillations in both training and validation loss during the entire training period. The rollout of 365 days leads to the most stable and smooth convergence.

We attribute this to the fact that a 365-day rollout covers the complete crop growth cycle, which enables ML components to learn complete seasonal dynamics in a single rollout. Although the rollout of 720 days also exhibits similarly stable convergence, the longer sequence length results in deeper computational graphs, increasing both memory usage and time costs of backpropagation. Therefore, we set a 365-day rollout as the default to train all NeuralCrop models.

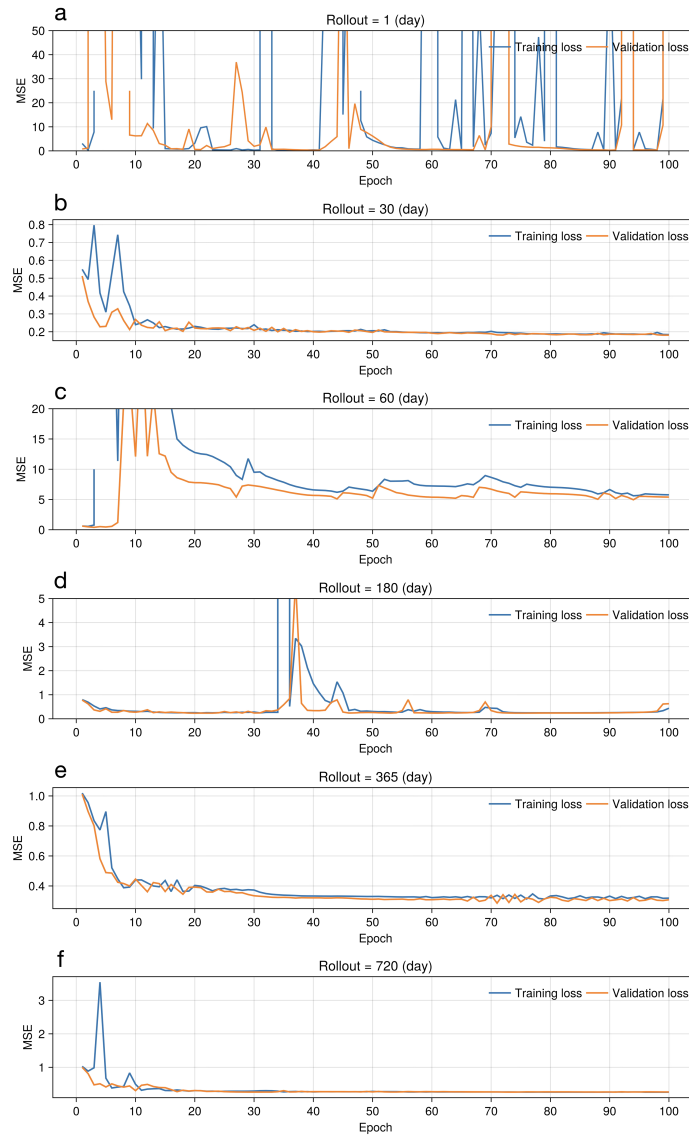


**Fig. S3** NeuralCrop models with identical model parameters trained on rollouts of 1, 30, 60, 180, 365, and 720 days (a-f).

## D.6 Output rescaling

All variables predicted by neural networks during training are rescaled using their historical minimum and maximum values over the training years, which prevents variables with large magnitudes from dominating the training. Specifically, for each predicted variable  $x$ , the normalized value  $\tilde{x}$  is computed as:

$$\tilde{x} = \frac{x - x_{\min}}{x_{\max} - x_{\min}}, \quad (\text{S26})$$

where  $x_{\min}$  and  $x_{\max}$  denote the minimum and maximum values of the variable, respectively.

## D.7 Training resources

All training and inference of NeuralCrop were conducted using a single NVIDIA H100 GPU with 80GB of memory.

We compared the efficiency of inference time between GPU-accelerated NeuralCrop and CPU-based LPJmL by running them on a  $0.5^\circ \times 0.5^\circ$  spatial resolution with daily time steps over a 20-year simulation period (7300 days) at different grid cells (Table S4). The LPJmL was running on one single AMD EPYC 9554 CPU with 128 cores and 768GB of memory. The results show that LPJmL takes over 7,500 seconds (about 2 hours) to simulate 14,157 grid cells, whereas NeuralCrop completes the exact simulation in 91 seconds, over 82 times faster. Similar gains appear at smaller grid cells, with 60 times faster for 7,865 grid cells and 16 times faster for 1,573 grid cells. Although GPU overhead makes the one-cell simulation slower, the efficiency increases rapidly with scale, reflecting the powerful parallel capacity of the GPU. This allows NeuralCrop to achieve competitive speed compared to traditional GGCM running on multiple CPU cores when doing global and daily simulations.

**Table S4** Inference time of GPU-accelerated NeuralCrop and CPU-based LPJmL simulating for a  $0.5^\circ \times 0.5^\circ$  spatial resolution with daily time steps over a 20-year simulation period (7300 days) at different grid cells. NeuralCrop was running on one single NVIDIA H100 GPU with 80GB of memory, and LPJmL was running on one single AMD EPYC 9554 CPU with 128 cores and 768GB of memory.

Grid cells	LPJmL	NeuralCrop	Times (speed up)
1	0.50 s	46.01 s	0.011x
1573	833.99 s	51.24 s	16.27x
7865	4169.94 s	70.02 s	59.55x
14157	7505.89 s	91.16 s	82.33x

## E Evaluation metrics

Evaluation metrics compare model simulations with ground truth. In this study, our preferred evaluation metrics include root mean square error (RMSE) and Pearson correlation coefficient ( $r$ ).

### E.1 Pearson correlation coefficient

Pearson correlation coefficient ( $r$ ) calculates the linear relationship between model simulations and observations. It is defined as:

$$r = \frac{\sum_{t=1}^T (y_t - \bar{y})(\hat{y}_t - \bar{\hat{y}})}{\sqrt{\sum_{t=1}^T (y_t - \bar{y})^2} \sqrt{\sum_{t=1}^T (\hat{y}_t - \bar{\hat{y}})^2}}, \quad (\text{S27})$$

where  $\hat{y}_t$  and  $y_t$  represent the simulated and observed values at time  $t$ , respectively, while  $\bar{\hat{y}}$  and  $\bar{y}$  denote their mean values. It ranges from  $-1$  to  $+1$ , with higher values indicating stronger agreement in the temporal variability. In particular,  $r$  is used to assess the ability of models to reproduce seasonal and interannual variations.

### E.2 Coefficient of determination

Coefficient of determination ( $R^2$ ) quantifies the proportion of the variance in the benchmark yield time series that is predictable from the model simulations, which is defined as the square of the Pearson correlation coefficient ( $r$ ) between the simulated and benchmark yields:

$$R^2 = r^2 \quad (\text{S28})$$

### E.3 Root mean square error

Root mean square error (RMSE) is a widely used metric to evaluate the accuracy of model predictions against observations. It is defined as the square root of the average of the squared differences between predicted values and observed values:

$$RMSE = \sqrt{\frac{1}{T} \sum_{t=1}^T (\hat{y}_t - y_t)^2}, \quad (\text{S29})$$

where  $\hat{y}_t$  is the model simulation at time  $t$ ,  $y_t$  is the corresponding observation, and  $T$  is the total number of time steps. A lower RMSE value indicates better agreement between model simulations and observations.

## F In situ validation

### F.1 In situ sites

To evaluate the performance of NeuralCrop across different crop types and environments, we conducted in situ validation using observational data from four crop flux tower sites (Table S5 and Fig. S4), selected to represent wheat, rice, corn, and soybean cropping regions. These are four global staple crops, spanning diverse climate zones, management practices, and phenological patterns, making them suitable cases for evaluating the performance of NeuralCrop. Each site provides high-quality daily eddy covariance measurements of carbon (i.e., GPP, RECO, and NEE) and soil water fluxes (SWC), as well as measurements of meteorological variables (Table S3).

**Table S5** Overview of crop flux tower sites used for NeuralCrop validation.

Site	Crop	Country	(latitude, longitude)	Year	Source
CH-Oe2 [25]	Wheat	Swiss	(47.2864, 7.7337)	2004-2023	ICOS
KR-CRK [26]	Rice	South Korea	(38.2013, 127.2506)	2005-2018	FLUXNET
US-Mo3 [27]	Soybean	USA	(39.2322, -92.1493)	2016-2021	AmeriFlux
US-Ne1 [28]	Corn	USA	(39.2322, -92.1493)	2001-2020	AmeriFlux

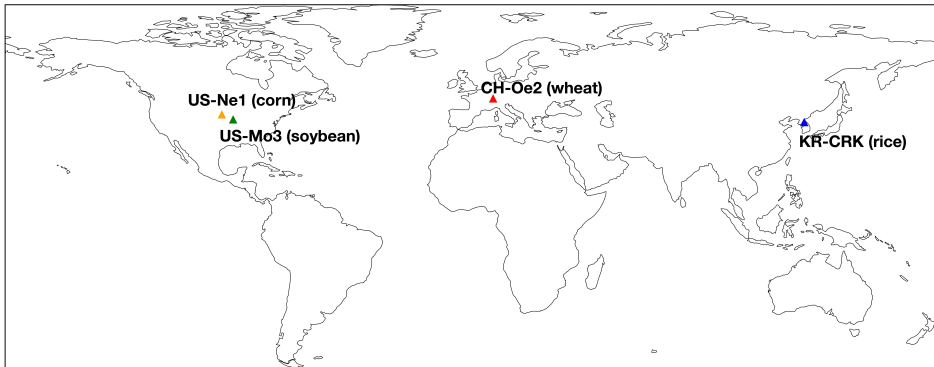


**Fig. S4** Geographical locations of the four FLUXNET sites used for in situ validation of NeuralCrop. Each site corresponds to a different crop: wheat (CH-Oe2), rice (KR-CRK), corn (US-Ne1), and soybean (US-Mo3).

### F.2 Training

We first train four NeuralCrop models for the above four crop sites separately using LPJmL outputs spanning from 2004 to 2017. Each NeuralCrop model is then fine-tuned with corresponding observational data (i.e., GPP, RECO, NEE, and SWC). The training setup can be found in Section C and Section D. Since crop rotation is practiced at these sites, we excluded flux data from non-target crop years and retained

only the data of periods during which the target crop was growing. We use the last year of data for validation and the remaining years for training (or fine-tuning). To evaluate the model performance, we use the root mean square error (RMSE, Eq. S29) and the Pearson correlation coefficient ( $r$ , Eq. S27) to assess both the accuracy and the ability of models to reproduce seasonal and interannual variations.

### F.3 Results

We compare the daily predictions of GPP, RECO, NEE, and SWC from NeuralCrop and LPJmL against FLUXNET observations across all four crop sites. Results indicate that NeuralCrop models outperform LPJmL models (see Figs. S5-S7 and Table S6). For GPP, NeuralCrop consistently achieves lower RMSE values (1.38–1.62) compared to LPJmL (2.06–2.85), with correlations up to 0.98, indicating a more accurate reproduction of seasonal cycles and peak flux magnitudes. Similarly, for RECO, NeuralCrop significantly reduces RMSE (0.89–1.74) relative to LPJmL (1.36–2.57), and achieves higher correlations (0.79–0.97 vs. 0.68–0.95), demonstrating its improved capability to capture respiration dynamics. For NEE, NeuralCrop not only yields smaller errors (1.15–1.66 vs. 1.66–2.73 for LPJmL) but also stronger correlations (0.90–0.95 vs. 0.83–0.94), highlighting its ability to better capture the timing and magnitude of transitions between carbon sink and source. For SWC, NeuralCrop reduces RMSE (14.51–37.30) relative to LPJmL (14.90–37.68) at all sites, while correlations are site-dependent with NeuralCrop outperforming LPJmL at KR-CRK but showing slightly lower correlations at the other sites.

Overall, these results suggest that NeuralCrop performs well across diverse crop types and climatic zones, with consistently better performance in carbon flux simulations and comparable performance in soil water simulations compared to the traditional process-based crop model LPJmL. The improved performance of NeuralCrop highlights its potential as a reliable tool for assessing the impacts of climate change on crop productivity.

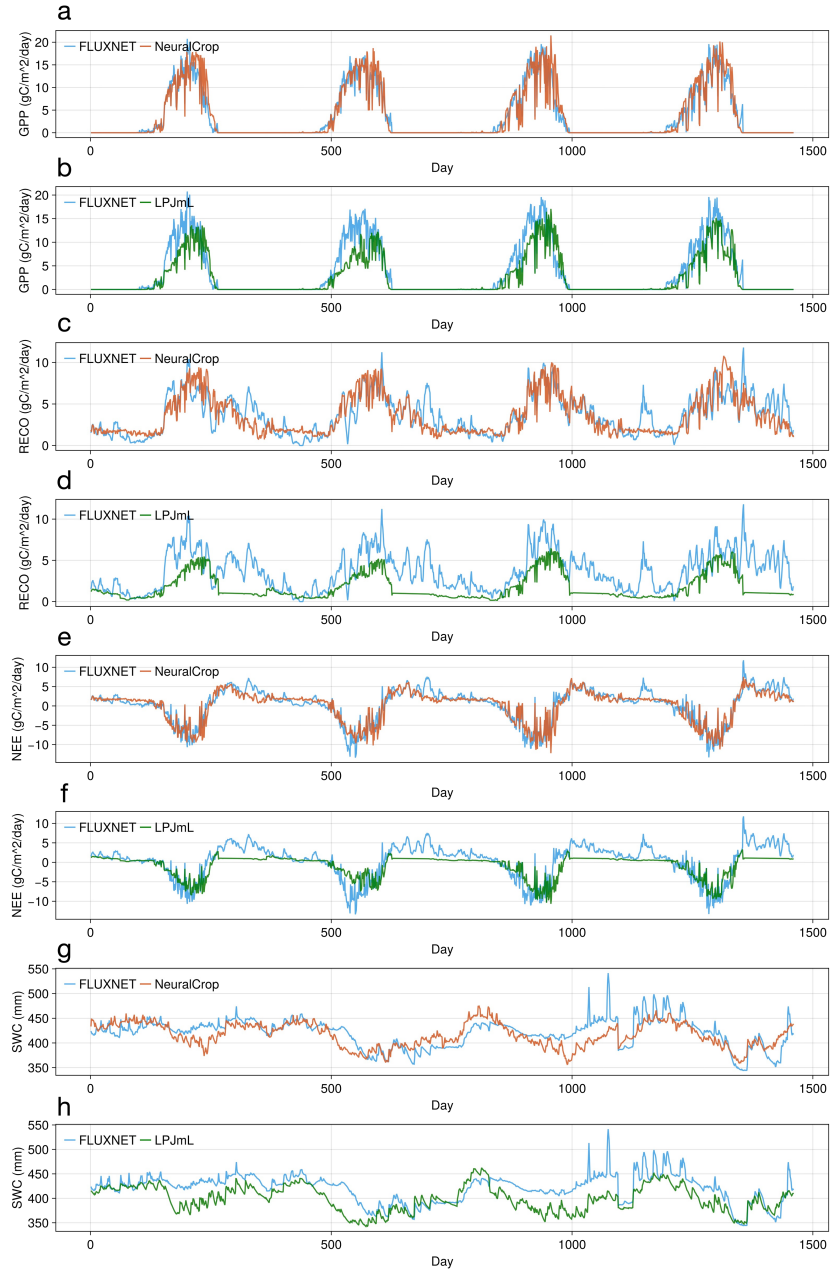


**Fig. S5** Comparison between FLUXNET observations and model simulations (NeuralCrop and LPJmL) for the wheat site (CH-Oe2) over four years. Time series are shown for (a–b) gross primary productivity (GPP,  $\text{gC m}^{-2} \text{ day}^{-1}$ ), (c–d) ecosystem respiration (RECO,  $\text{gC m}^{-2} \text{ day}^{-1}$ ), (e–f) net ecosystem exchange (NEE,  $\text{gC m}^{-2} \text{ day}^{-1}$ ), and (g–h) soil water content (SWC, mm). Panels (a, c, e, g) compare FLUXNET with NeuralCrop, while panels (b, d, f, h) compare FLUXNET with LPJmL. Blue lines represent FLUXNET data, red lines represent NeuralCrop simulations, and green lines represent LPJmL simulations.

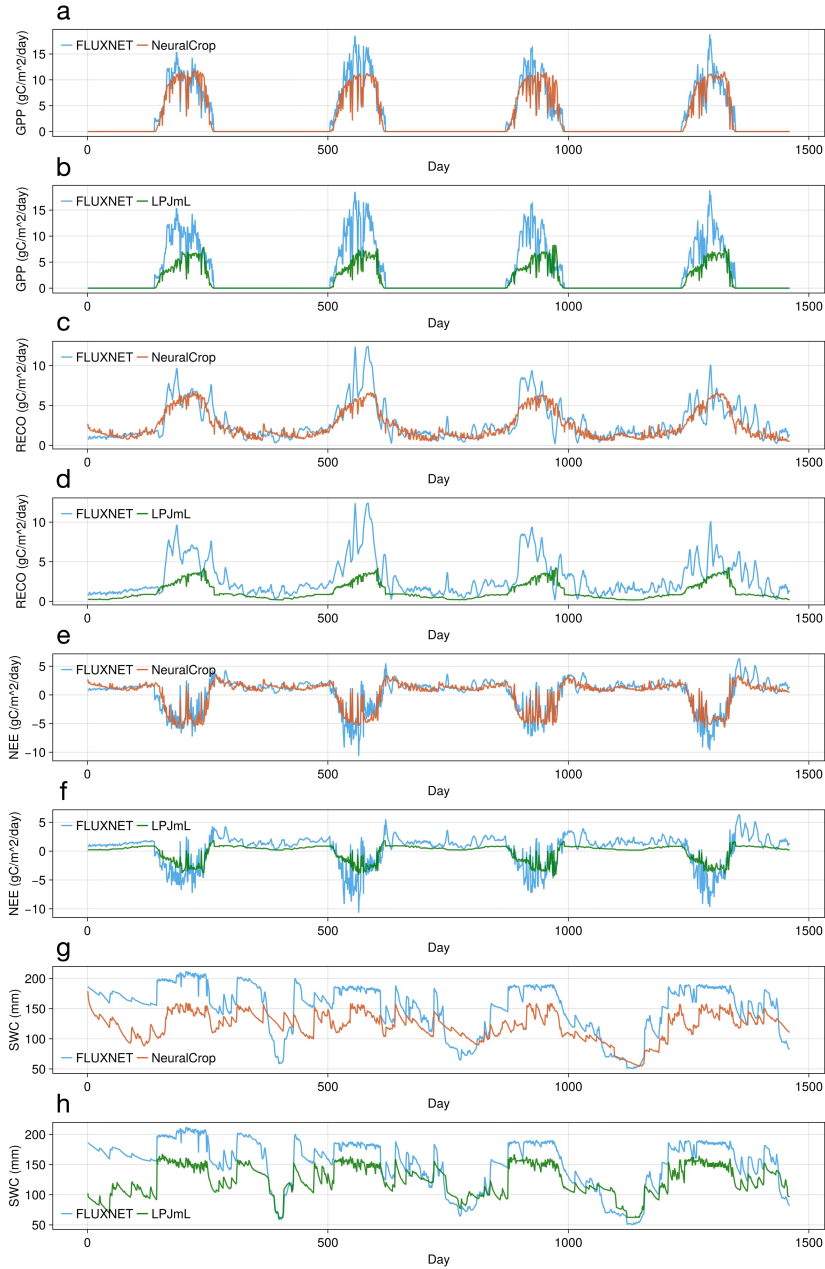


**Fig. S6** Comparison between FLUXNET observations and model simulations (NeuralCrop and LPJmL) for the rice site (KR-CRK) over four years. Time series are shown for (a–b) gross primary productivity (GPP,  $\text{gC m}^{-2} \text{day}^{-1}$ ), (c–d) ecosystem respiration (RECO,  $\text{gC m}^{-2} \text{day}^{-1}$ ), (e–f) net ecosystem exchange (NEE,  $\text{gC m}^{-2} \text{day}^{-1}$ ), and (g–h) soil water content (SWC, mm). Panels (a, c, e, g) compare FLUXNET with NeuralCrop, while panels (b, d, f, h) compare FLUXNET with LPJmL. Blue lines represent FLUXNET data, red lines represent NeuralCrop simulations, and green lines represent LPJmL simulations.

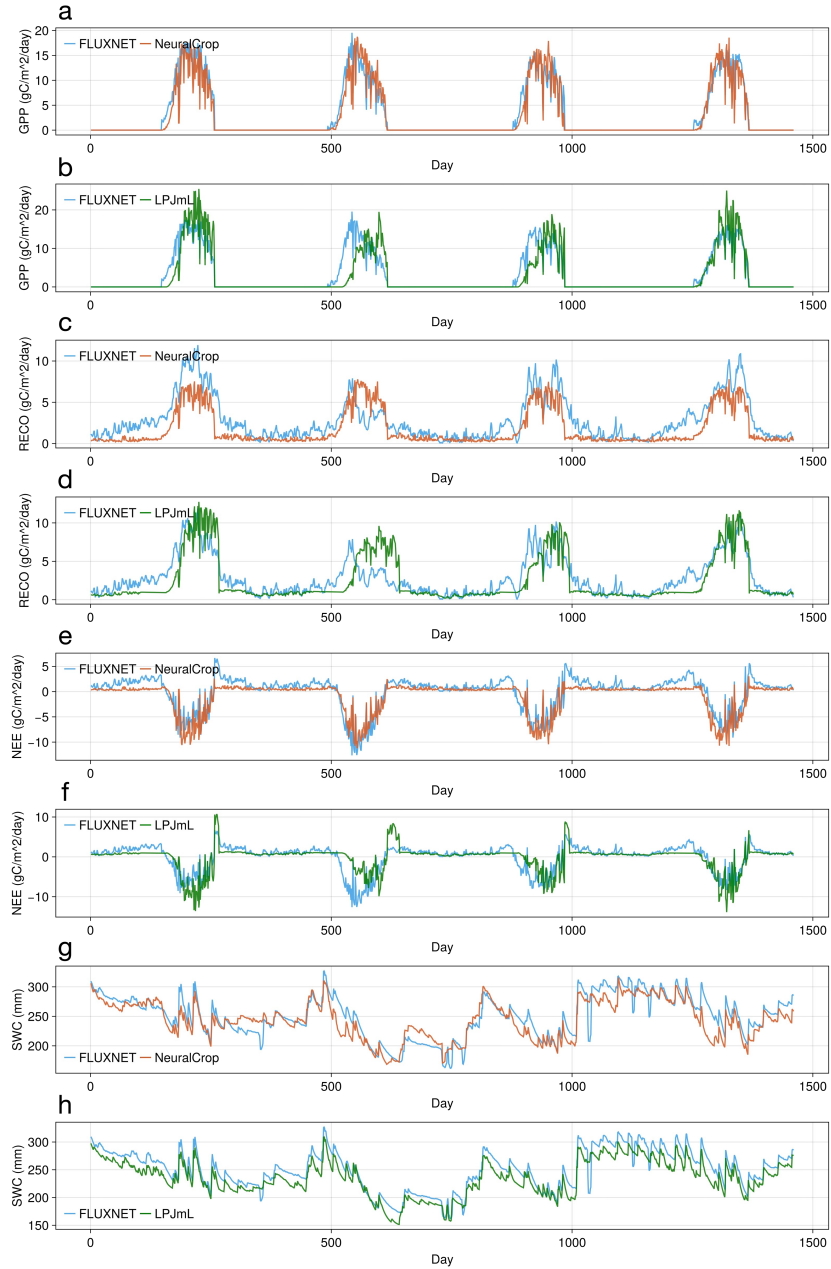


**Fig. S7** Comparison between FLUXNET observations and model simulations (NeuralCrop and LPJmL) for the soybean site (US-Mo3) over four years. Time series are shown for (a–b) gross primary productivity (GPP,  $\text{gC m}^{-2} \text{ day}^{-1}$ ), (c–d) ecosystem respiration (RECO,  $\text{gC m}^{-2} \text{ day}^{-1}$ ), (e–f) net ecosystem exchange (NEE,  $\text{gC m}^{-2} \text{ day}^{-1}$ ), and (g–h) soil water content (SWC, mm). Panels (a, c, e, g) compare FLUXNET with NeuralCrop, while panels (b, d, f, h) compare FLUXNET with LPJmL. Blue lines represent FLUXNET data, red lines represent NeuralCrop simulations, and green lines represent LPJmL simulations.

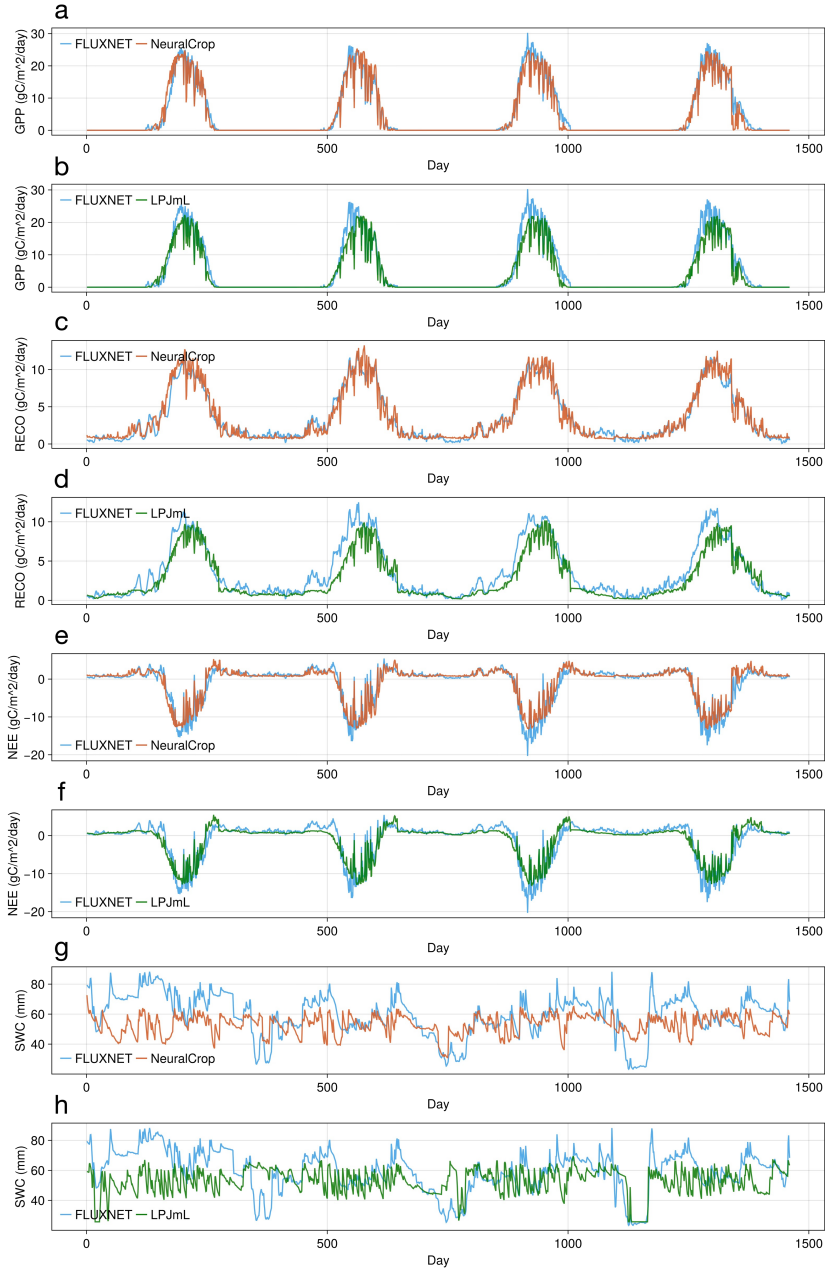


**Fig. S8** Comparison between FLUXNET observations and model simulations (NeuralCrop and LPJmL) for the corn site (US-Ne1) over four years. Time series are shown for (a–b) gross primary productivity (GPP,  $\text{gC m}^{-2} \text{day}^{-1}$ ), (c–d) ecosystem respiration (RECO,  $\text{gC m}^{-2} \text{day}^{-1}$ ), (e–f) net ecosystem exchange (NEE,  $\text{gC m}^{-2} \text{day}^{-1}$ ), and (g–h) soil water content (SWC, mm). Panels (a, c, e, g) compare FLUXNET with NeuralCrop, while panels (b, d, f, h) compare FLUXNET with LPJmL. Blue lines represent FLUXNET data, red lines represent NeuralCrop simulations, and green lines represent LPJmL simulations.

**Table S6** Model performance against FLUXNET observations at four crop sites: CH-Oe2 (wheat), KR-CRK (rice), US-Mo3 (soybean), and US-Ne1 (corn). Performance metrics include Root Mean Square Error (RMSE) and Pearson correlation coefficient ( $r$ ), calculated for gross primary productivity (GPP), ecosystem respiration (RECO), net ecosystem exchange (NEE), and soil water content (SWC). Bold numbers indicate the better performance between NeuralCrop and LPJmL.

Variable	Metric	Wheat (CH-Oe2)		Rice (KR-CRK)		Soybean (US-Mo3)		Corn (US-Ne1)	
		NeuralCrop	LPJmL	NeuralCrop	LPJmL	NeuralCrop	LPJmL	NeuralCrop	LPJmL
GPP	RMSE	<b>1.53</b>	2.51	<b>1.42</b>	2.83	<b>1.38</b>	2.85	<b>1.62</b>	2.06
	$r$	<b>0.96</b>	0.91	<b>0.95</b>	0.90	<b>0.96</b>	0.86	<b>0.98</b>	0.97
RECO	RMSE	<b>1.51</b>	2.57	<b>1.37</b>	2.37	<b>1.74</b>	1.82	<b>0.89</b>	1.36
	$r$	<b>0.79</b>	0.68	<b>0.83</b>	0.77	<b>0.82</b>	0.80	<b>0.97</b>	0.95
NEE	RMSE	<b>1.66</b>	2.73	<b>1.15</b>	1.68	<b>1.57</b>	2.28	<b>1.53</b>	1.66
	$r$	<b>0.92</b>	0.83	<b>0.90</b>	0.87	<b>0.90</b>	0.74	<b>0.95</b>	0.94
SWC	RMSE	<b>22.21</b>	30.58	<b>37.30</b>	37.68	<b>17.55</b>	17.88	<b>14.51</b>	14.90
	$r$	0.67	<b>0.68</b>	<b>0.62</b>	0.53	0.87	<b>0.89</b>	0.32	<b>0.34</b>

## G Large-scale cropping regions

### G.1 European wheat

#### G.1.1 Subnational crop statistics

We use the harmonized EU subnational crop statistics dataset [29] as ground truth, which was collected from National Statistical Institutes (NSIs) in EU countries and the EUROSTAT dataset. This dataset provides primarily county-level, and state-level in some EU countries, records of production, area, and yield in wheat, including soft, durum, and total wheat, across 27 EU countries over the period 1975–2020. We used the total wheat statistics from 2000 to 2019 for model evaluation, which includes 14,910 records for yield, covering a total of 883 regions (specifically, 3 NUTS-1, 69 NUTS-2, and 811 NUTS-3 statistical regions). In official statistics, wheat yields are reported at the standard EU humidity (14%). To ensure consistency with model simulations, all reported wheat yields are converted to dry matter (0% humidity) prior to analysis, as follows:

$$Y_{\text{DM}} = Y_{\text{HM}} \times (1 - h), \quad (\text{S30})$$

where  $Y_{\text{DM}}$  is the yield at 0% humidity,  $Y_{\text{HM}}$  is the yield at the standard humidity, and  $h$  is the standard humidity fraction.

#### G.1.2 Pre-training

In the European wheat cropping regions, we pre-trained NeuralCrop models using LPJmL outputs from 2016-1-1 to 2017-12-31 to simulate winter wheat varieties under rain-fed and irrigated management conditions, and outputs from 2016-1-1 to 2016-12-31 to simulate spring wheat varieties under rain-fed and irrigated management conditions, respectively. The initial states of the NeuralCrop models were derived from the LPJmL simulations on the last day of 2015, ensuring consistent soil water, carbon, and nitrogen conditions at the beginning of the training period. The training setup can be found in Section C and Section D.

To ensure the pre-trained NeuralCrop is adequately prepared for the subsequent fine-tuning phase, we compared simulated wheat yields from NeuralCrop and LPJmL for the period 2000-2019 at the subnational level. The simulated yields are aggregated to subnational units using an area-weighted average method, described in Section H.1. Fig. S9 shows that pre-trained NeuralCrop and LPJmL exhibit a strong agreement in their simulated wheat yields at the subnational level. The correlation coefficients are consistently high (mean values predominantly above 0.8) across all EU countries. This robust correlation confirms that the pre-trained NeuralCrop effectively learned and reproduced the wheat yield behavior of LPJmL.

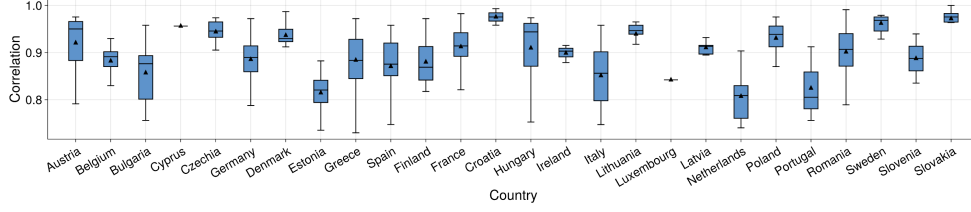


**Fig. S9** Boxplots of time series correlation coefficient of simulated wheat yields between pre-trained NeuralCrop and LPJmL at the subnational level, aggregated by country for the period 2000–2019, with countries ordered alphabetically by their country code (A–Z). The box boundaries represent the interquartile range (IQR), defined by the first quartile, the median, and the third quartile. The upper and lower whiskers represent the maximum and minimum values that are within 1.5 times the interquartile range of the box. The black triangles are the mean value.

### G.1.3 Fine-tuning

NeuralCrop models were further fine-tuned using site-level eddy-covariance flux tower data across major European wheat cropping regions. The wheat flux data comprised 12 flux tower sites distributed in Belgium, Switzerland, Germany, France, and Italy (see Table S7 and Fig. S10), covering a broad range of climatic and management conditions. These observations provide daily GPP, RECO, NEE, and, for most sites, SWC, as well as auxiliary meteorological variables, spanning from 2001 to 2023. Since crop rotation is practiced at most sites, we excluded flux data from non-target crop years and retained only the data of periods during which the wheat was growing. The final dataset included a total of 76 site-years of wheat flux observations for fine-tuning.

**Table S7** Overview of European wheat flux tower sites used for fine-tuning of NeuralCrop.

Site	Country	(latitude, longitude)	Year	Source
BE-Lon [30]	Belgium	(50.5516, 4.7462)	2004-2020	ICOS
CH-Oe2 [25]	Switzerland	(47.2864, 7.7337)	2004-2023	ICOS
DE-Geb [31]	Germany	(51.0997, 10.9146)	2001-2020	ICOS
DE-Kli [32]	Germany	(50.8930, 13.5223)	2004-2023	ICOS
DE-RuS [33]	Germany	(50.8659, 6.4471)	2011-2014	ICOS
DE-Seh [34]	Germany	(50.8706, 6.4497)	2001-2010	FLUXNET
DK-Vng [35]	Germany	(56.0374, 9.1607)	2009-2018	ICOS
FR-Gri [36]	France	(48.8442, 1.9519)	2004-2014	FLUXNET
FR-Aur [37]	France	(43.5496, 1.1061)	2005-2023	ICOS
FR-EM2 [38]	France	(49.8721, 3.0206)	2017-2023	ICOS
FR-Lam [39]	France	(43.4964, 1.2378)	2005-2020	ICOS
IT-CA2 [40]	Italy	(42.3772, 12.0260)	2011-2014	ICOS



**Fig. S10** Geographical locations of the EU wheat flux tower sites used for fine-tuning of NeuralCrop.

## G.2 US Corn Belt

### G.2.1 County-level crop statistics

In this study, the US Corn Belt includes the states of South Dakota, Minnesota, Iowa, Missouri, Illinois, Indiana, Ohio, Michigan, and Wisconsin (shown in Fig. S11) [41]. County-level corn statistics from National Agricultural Statistics Service of USDA are used as ground truth, which provides records of production, area, and yield in corn, starting from 1910. We used the corn statistics from 2000 to 2019 for model evaluation, which includes 13,665 records for yield, covering a total of 764 counties. We also use the Eq. G.1.1, with  $h = 0.155$ , to convert the reported corn yields to dry matter (0% humidity) before analysis.

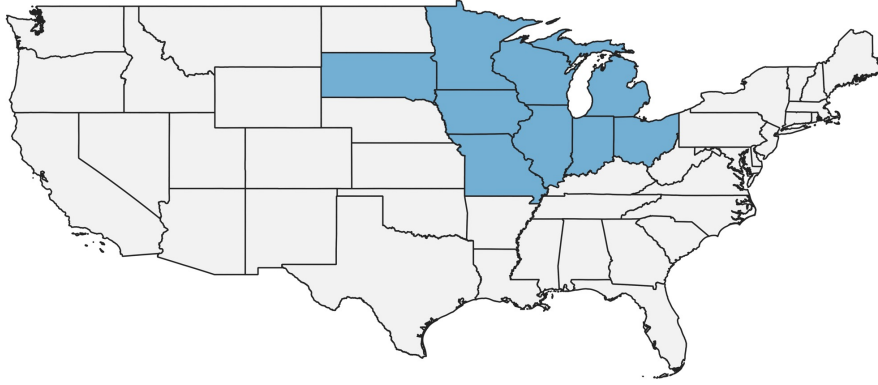


**Fig. S11** States shaded in blue represent the US Corn Belt, including the states of South Dakota, Minnesota, Iowa, Missouri, Wisconsin, Illinois, Michigan, Indiana, and Ohio.

### G.2.2 Pre-training

In the US Corn Belt cropping regions, we pre-trained NeuralCrop models using LPJmL outputs from 2016-1-1 to 2016-12-31 to simulate corn under rain-fed and irrigated management conditions, respectively. The initial states of the NeuralCrop models were derived from the LPJmL simulations on the last day of 2015, ensuring consistent soil water, carbon, and nitrogen conditions at the beginning of the training period. The training setup can be found in Section C and Section D.

Same to EU wheat pre-training, we compared simulated corn yields from NeuralCrop and LPJmL for the period 2000-2019 at the county level. The simulated yields are aggregated to counties using an area-weighted average method, described in H.1. Fig. S12 shows that pre-trained NeuralCrop and LPJmL exhibit a strong agreement in their simulated corn yields at the county level. The correlation coefficients are consistently high (mean values predominantly above 0.8) across all states of US Corn Belt. This robust correlation confirms that the pre-trained NeuralCrop effectively learned and reproduced the corn yield behavior of LPJmL.

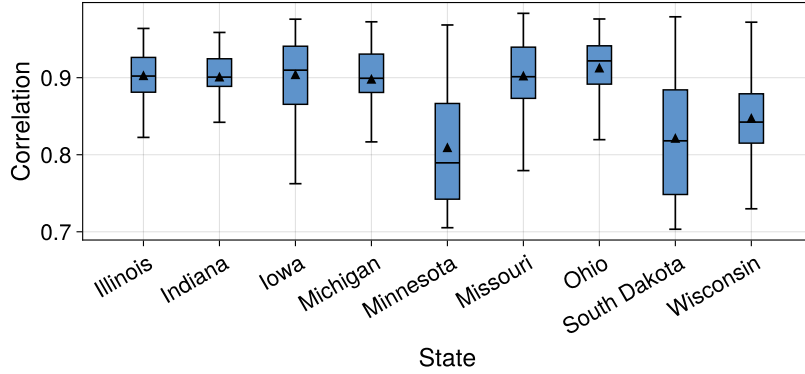


**Fig. S12** Boxplots of time series correlation coefficient of simulated corn yields between pre-trained NeuralCrop and LPJmL at the county level, aggregated by state for the period 2000–2019. The box boundaries represent the interquartile range (IQR), defined by the first quartile, the median, and the third quartile. The upper and lower whiskers represent the maximum and minimum values that are within 1.5 times the interquartile range of the box. The black triangles are the mean value.

### G.2.3 Fine-tuning

NeuralCrop models were further fine-tuned using site-level eddy-covariance flux tower data across major US corn cropping regions. The corn flux data comprised 10 flux tower sites distributed in the states of Missouri, Nebraska, Minnesota, and California (Table S8 and Fig. S13), covering a broad range of climatic and management conditions. These observations provide daily GPP, RECO, NEE, and, for most sites, SWC, as well as auxiliary meteorological variables, spanning from 2001 to 2023. Since crop rotation is practiced at most sites, we excluded flux data from non-target crop years and retained only the data of periods during which the corn was growing. Finally, the dataset included 26 site-years of corn flux observations for fine-tuning.

**Table S8** Overview of US corn flux tower sites used for fine-tuning of NeuralCrop.

Site	(latitude, longitude)	Year	Source
US-Bi2 [42]	(38.1091, -121.5351)	2017-2021	AmeriFlux
US-Mo1 [43]	(39.2298, -92.1167)	2015-2023	AmeriFlux
US-Mo3 [44]	(39.2322, -92.1493)	2016-2021	AmeriFlux
US-Ne1 [28]	(41.1651, -96.4766)	2001-2020	AmeriFlux
US-Ne2 [45]	(41.1649, -96.4701)	2001-2013	AmeriFlux
US-Ne3 [46]	(41.1797, -96.4397)	2001-2013	AmeriFlux
US-Ro1 [47]	(44.7143, -93.0898)	2004-2016	AmeriFlux
US-Ro3 [48]	(44.7217, -93.0893)	2004-2007	AmeriFlux
US-Ro5 [49]	(44.6910, -93.0576)	2017-2023	AmeriFlux
US-Ro6 [50]	(44.6946, -93.0578)	2017-2023	AmeriFlux

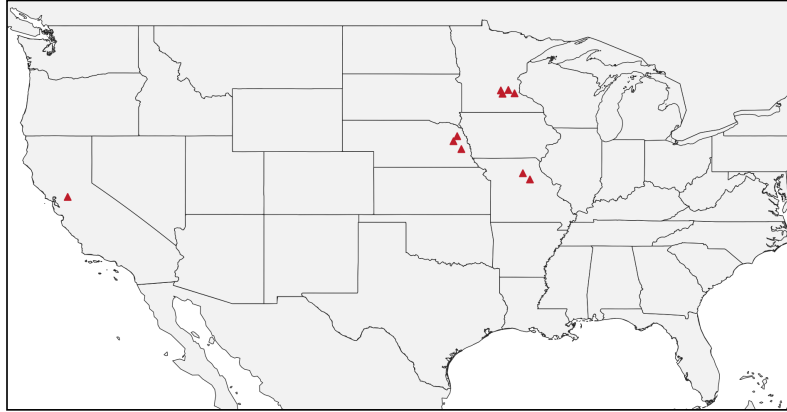


**Fig. S13** Geographical locations of the US corn flux tower sites used for fine-tuning NeuralCrop.

### G.3 Out-of-sample generalization

Pure ML models typically exhibit poor performance in out-of-sample conditions, and even produce physically inconsistent predictions. We anticipate that NeuralCrop may generalize well in unseen conditions because of its hybrid modelling approach, where neural networks are used only to replace or augment selected sub-processes while simultaneously being constrained by other, explicitly resolved processes. To validate this hypothesis, we compared NeuralCrop with pure ML models (i.e., neural networks in the form of multi-layer perceptrons) that were trained on the European wheat cropping regions and used to simulate the US wheat cropping regions (including the states of Montana, North Dakota, South Dakota, Nebraska, Colorado, Kansas, Oklahoma, and Texas) (Fig. S15), respectively, a scenario entirely unseen during training. The simulated wheat yields are aggregated from the  $0.5^\circ \times 0.5^\circ$  (latitude  $\times$  longitude) grid to the county level using area-weighted averaging, as shown in H.1. Results demonstrate that NeuralCrop presents robust spatial generalization capabilities, even outperforming the fully process-based LPJmL model in six out of eight states, with comparable performance in the remaining two (Fig. S14). In contrast, the pure ML model shows significantly weaker predictive skills across all states. This indicates that our hybrid NeuralCrop model provides a promising approach for accurate simulation of large-scale agricultural systems where observational data is scarce.

The European wheat statistics were downloaded from <https://data.jrc.ec.europa.eu/dataset/685949ff-56de-4646-a8df-844b5bb5f835>, which provides annual wheat statistics on area, production, and average yield across three levels of the Nomenclature of Territorial Units for Statistics (NUTS). The US wheat statistics were obtained from <https://quickstats.nass.usda.gov/>.

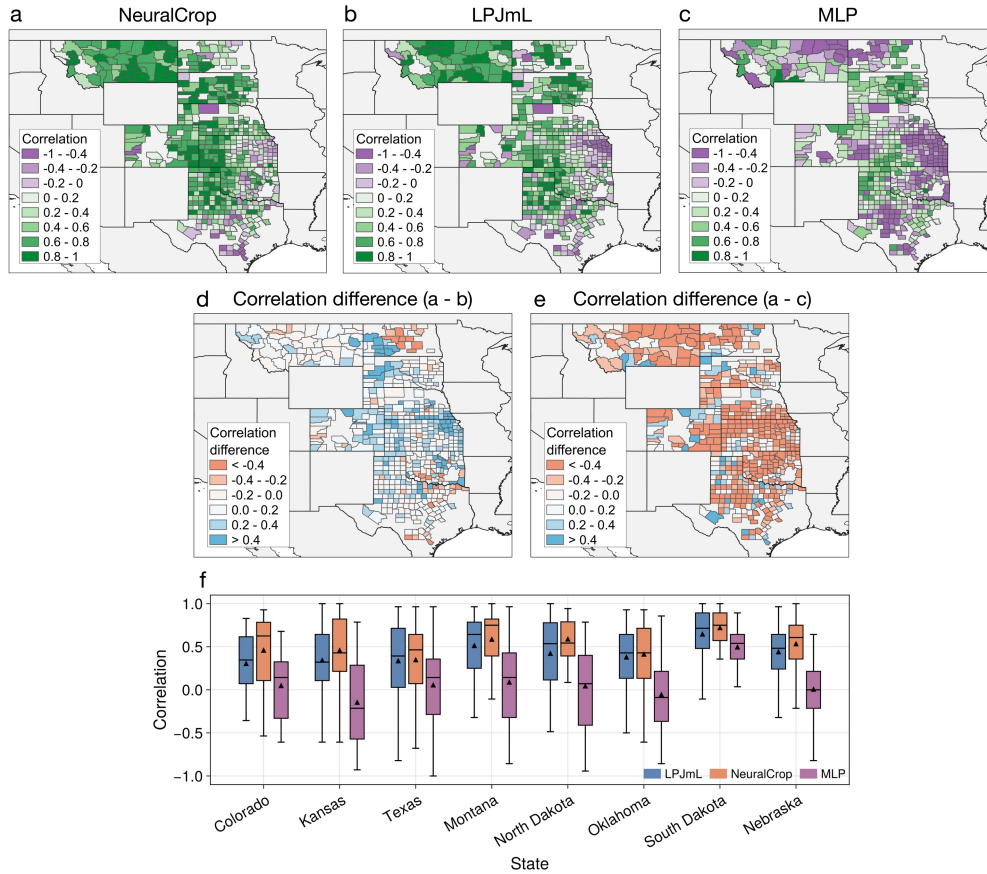


**Fig. S14** Comparison of simulated wheat yields from NeuralCrop, LPJmL, and MLP with USDA statistics in the US Corn Belt, including nine states, including eight states (i.e., Montana, North Dakota, South Dakota, Nebraska, Colorado, Kansas, Oklahoma, and Texas). Simulated wheat yields are aggregated from the  $0.5^\circ \times 0.5^\circ$  (latitude  $\times$  longitude) grid to the county level using area-weighted averaging. **a**, Time series correlation coefficient between NeuralCrop simulated corn yield and USDA statistics at the county level for the period 2000-2007 (range from  $-1$  to  $1$ , darker green areas indicate stronger positive correlations, and darker purple areas indicate stronger negative correlations). **b**, Same as panel a, but for LPJmL. **c**, Same as panel a, but for MLP. **d**, The difference of correlation coefficients between NeuralCrop and LPJmL (i.e., panel a – panel b), where blue areas indicate regions where NeuralCrop outperforms LPJmL in simulating interannual yield variability, and red areas indicate regions where LPJmL performs better. **e**, Same as panel d, but for the difference between NeuralCrop and MLP (i.e., panel a – panel c). **f**, Boxplots of time series correlation coefficients between simulated wheat yield and USDA statistics at the county level, aggregated by states for the period 2000-2007. Blue boxes represent LPJmL, orange boxes represent NeuralCrop, and green boxes represent MLP. The box boundaries represent the interquartile range (IQR), defined by the first quartile, the median, and the third quartile. The upper and lower whiskers represent the maximum and minimum values that are within 1.5 times the interquartile range of the box. The black triangles are the mean value.

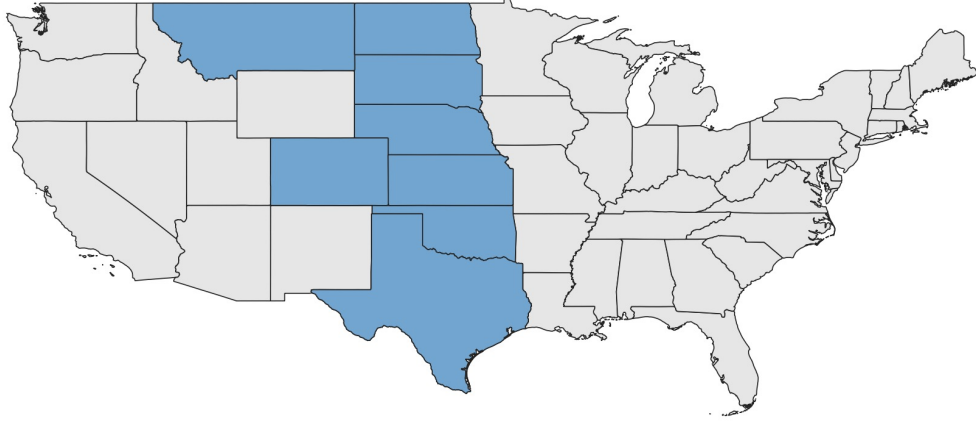


**Fig. S15** States shaded in blue represent the US main wheat regions, including the states of Montana, North Dakota, South Dakota, Nebraska, Colorado, Kansas, Oklahoma, and Texas.

#### G.4 SPEI

The Standardized Precipitation Evapotranspiration Index (SPEI) is a drought index that combines precipitation ( $P$ ) and potential evapotranspiration ( $PET$ ) [51]. It can be used to characterize drought intensity, duration, and frequency across different timescales, thereby providing a consistent framework to assess water availability impacts on agriculture. SPEI is defined as the difference between  $P_t$  and  $PET_t$  at time  $t$ :

$$D_t = P_t - PET_t, \quad (\text{S31})$$

where  $PET_t$  is calculated using Priestley-Taylor equation, following LPJmL scheme [10]. The accumulated water balance over a timescale of  $k$  months is then given by:

$$D_{t,k} = \sum_{i=0}^{k-1} (P_{t-i} - PET_{t-i}), \quad (\text{S32})$$

where  $D_{t,k}$  represents the climatic water balance integrated over  $k$  months. The series  $D_{t,k}$  is fitted to a probability distribution (typically Logistic) and transformed into a standardized normal variable with mean zero and unit variance. The standardized index is expressed as:

$$\text{SPEI}_{t,k} = \frac{D_{t,k} - \mu}{\sigma}, \quad (\text{S33})$$

where  $\mu$  and  $\sigma$  are the mean and standard deviation of the fitted distribution, respectively. Negative values of  $\text{SPEI}_{t,k}$  indicate drier conditions than normal, while positive values indicate wetter conditions than normal.

In this study, SPEI is calculated using an accumulation period of  $k = 3$  months. We select SPEI during key crop growth stages to assess water availability relevant to crop production. Based on calculated SPEI values, drought severity is categorized into four classes:

**Table S9** Dryness classification based on SPEI.

Value	Classification
$1.5 \leq \text{SPEI} \leq \infty$	Extremely Wet
$1.0 \leq \text{SPEI} \leq 1.5$	Very Wet
$0.5 \leq \text{SPEI} \leq 1.0$	Moderately Wet
$-0.5 \leq \text{SPEI} \leq 0.5$	Normal
$-1.0 \leq \text{SPEI} < -0.5$	Moderately Dry
$-1.5 \leq \text{SPEI} < -1.0$	Very Dry
$-\infty \leq \text{SPEI} < -1.5$	Extremely Dry

## H Yield data processing

### H.1 Yield aggregation

NeuralCrop and LPJmL simulate yields on a global grid at  $0.5^\circ \times 0.5^\circ$  (latitude  $\times$  longitude) spatial resolution, whereas reported yields are usually available at the county level or for even larger administrative units. To make the simulated yields comparable with these observations, we first linearly downscale the  $0.5^\circ$  outputs to a finer  $0.05^\circ$  grid by uniformly assigning the original cell value to all sub-cells, and then aggregate the  $0.05^\circ$  yields to target regions using the harvested-area weighted method, see below.

Let  $H_{j,t}$  denote the harvested area of the target crop in  $0.05^\circ$  grid  $j$  and year  $t$ . For a region  $r$  (e.g., county, state, or country), the harvested-area weighted mean yield  $\bar{y}_{r,t}$  is computed as

$$\bar{y}_{r,t} = \sum_{j \in r} \alpha_{j,t} y_{j,t}^{0.05}, \quad \alpha_{j,t} = \frac{H_{j,t}}{\sum_{j \in r} H_{j,t}}, \quad (\text{S34})$$

where  $\alpha_{j,t}$  is the fraction of the regional harvested area located in grid cell  $j$ .

### H.2 Yield detrending

To remove the effects of long-term improvements associated with crop breeding and management while retaining interannual variability primarily driven by climate fluctuations, we use smoothing splines to detrend the simulated and observed yield time series. Given time series  $(t, y_t)$ ,  $t = 1, 2, \dots, T$ , where  $t$  denotes the year and  $y_t$  represents the corresponding crop yield (either simulated or observed), the smoothing spline estimate  $\hat{f}(x)$  of the function  $f(t)$  is obtained by minimizing the following objective function:

$$\sum_{i=1}^T (y_t - f(t))^2 + \lambda \int [f''(t)]^2 dt, \quad (\text{S35})$$

where the first term,  $\sum_{i=1}^T (y_t - f(t))^2$ , measures the lack of fit to the data, the second term,  $\int [f''(t)]^2 dt$ , penalizes curvature of the function, thereby enforcing smoothness, and  $\lambda$  ( $\geq 0$ ) is the smoothing parameter, which controls the trade-off between goodness of fit and smoothness. The optimal solution  $f(x)$  is a cubic spline function. As  $\lambda \rightarrow 0$ , the solution approaches an interpolating spline, exactly passing through all data points. As  $\lambda \rightarrow \infty$ , the solution converges to a linear function, representing complete smoothing. In this study, the smoothing parameter  $\lambda$  is selected empirically based on the characteristics of the yield time series. The detrended yield time series is then obtained as:

$$y_t^{\text{detrended}} = y_t - \hat{f}(t). \quad (\text{S36})$$

### H.3 Yield anomalies

Yield anomalies are calculated to measure the relative deviation of annual yields from their long-term trends. Specifically, given the simulated or observed yield  $y_t$  in year  $t$  and the corresponding expected yield  $\hat{f}(t)$  estimated by a smoothing spline function (Section H.2), the normalized yield anomaly is defined as:

$$\hat{a}_t = \frac{y_t - \hat{f}(t)}{\hat{f}(t)}. \quad (\text{S37})$$

# I Additional information

## I.1 Case study

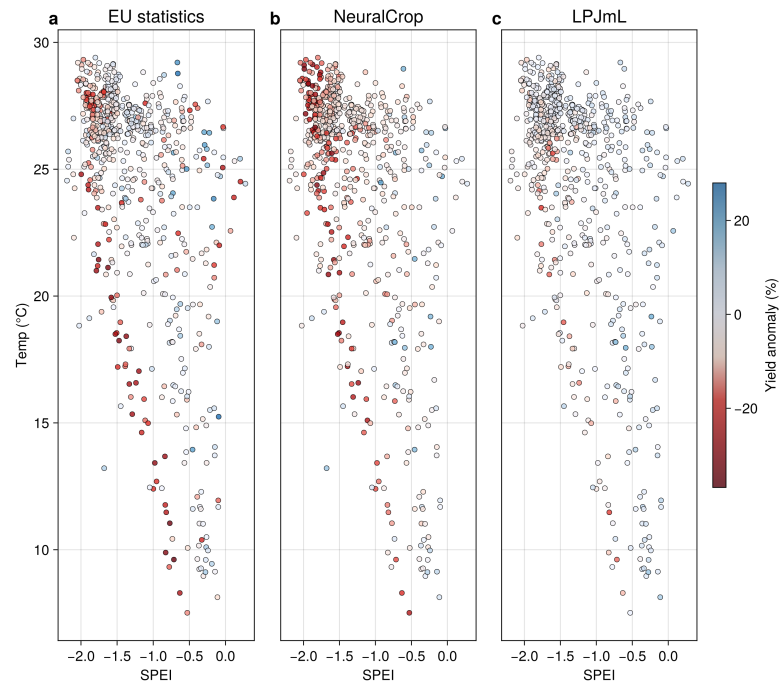


**Fig. S16** Wheat yield anomaly patterns across compound drought–heat conditions in European wheat regions during the 2018 drought. **a–c**, Scatter plots of wheat yield anomaly (%) versus Standardized Precipitation Evapotranspiration Index (SPEI) and growing-season maximum temperature for (a) EU statistics, (b) NeuralCrop, and (c) LPJmL at the subnational level. Point colors represent yield anomalies, with red indicating negative anomalies (yield losses) and blue indicating positive anomalies (yield gains).

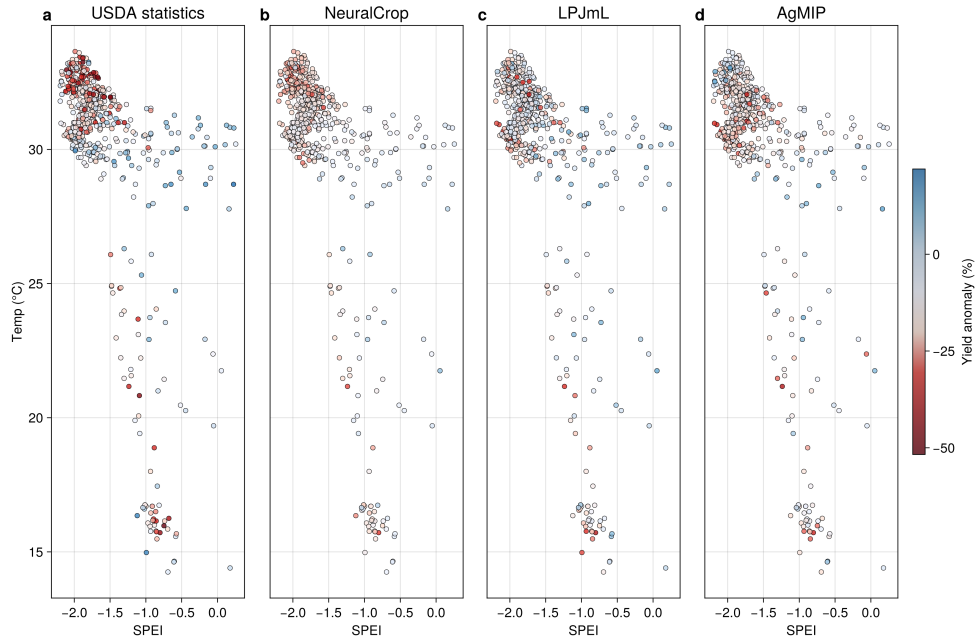


**Fig. S17** Wheat yield anomaly patterns across compound drought–heat conditions in the US Corn Belt during the 2012 drought. **a–d**, Scatter plots of wheat yield anomaly (%) versus SPEI and growing-season maximum temperature for (a) USDA statistics, (b) NeuralCrop, (c) LPJmL, and (d) the AgMIP (the ensemble median of 8 GGCMs) at the county level. Point colors represent yield anomalies, with red indicating negative anomalies (yield losses) and blue indicating positive anomalies (yield gains).

## I.2 France wheat anomalies in 2016

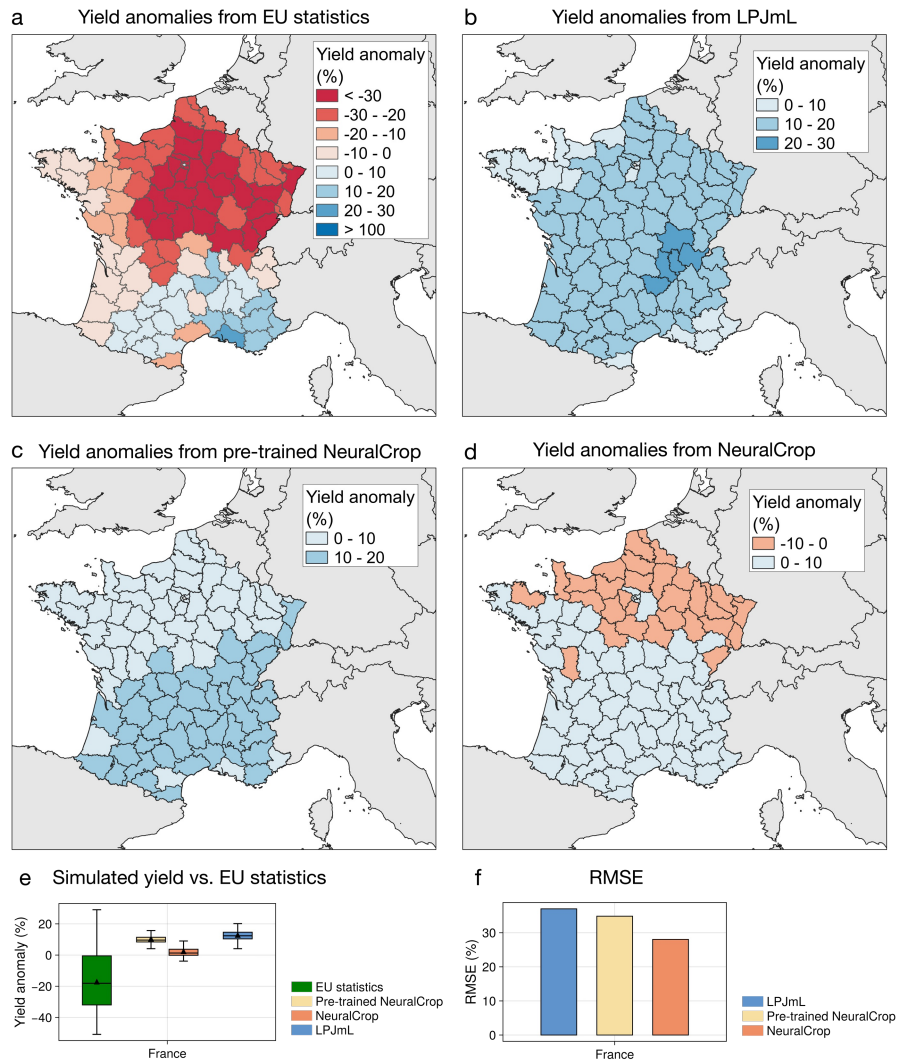


**Fig. S18** Wheat yield anomalies and model performance for NeuralCrop and LPJmL under the 2016 heavy rainfall in France. **a**, Wheat yield anomalies in 2016 at the subnational level from EU statistics. **b**, Wheat yield anomalies in 2016 at the subnational level from LPJmL. **c**, Wheat yield anomalies in 2016 at the subnational level from pre-trained NeuralCrop. **d**, Wheat yield anomalies in 2016 at the subnational level from NeuralCrop. **e**, Boxplots of 2016 wheat yield anomalies (%). The green box denotes EU statistics, the yellow box denotes pre-trained NeuralCrop, the orange box denotes NeuralCrop, and the blue box denotes LPJmL. The upper and lower whiskers represent the maximum and minimum values that are within 1.5 times the interquartile range of the box. The black triangles are the mean value. **f**, Root mean square error (RMSE) between simulated 2016 yield anomalies and EU statistics. The yellow box denotes pre-trained NeuralCrop, the orange box denotes NeuralCrop, and the blue box denotes LPJmL.

## References

- [1] Ricky TQ Chen, Yulia Rubanova, Jesse Bettencourt, and David K Duvenaud. Neural ordinary differential equations. *Advances in neural information processing systems*, 31, 2018.
- [2] Jeff Bezanson, Alan Edelman, Stefan Karpinski, and Viral B Shah. Julia: A fresh approach to numerical computing. *SIAM review*, 59(1):65–98, 2017.
- [3] Christopher Rackauckas, Yingbo Ma, Julius Martensen, Collin Warner, Kirill Zubov, Rohit Supekar, Dominic Skinner, Ali Ramadhan, and Alan Edelman. Universal differential equations for scientific machine learning. *arXiv preprint arXiv:2001.04385*, 2020.
- [4] Avik Pal. Lux: Explicit Parameterization of Deep Neural Networks in Julia, April 2023. If you use this software, please cite it as below.
- [5] Avik Pal. On Efficient Training & Inference of Neural Differential Equations, 2023.
- [6] Michael Innes. Don’t unroll adjoint: Differentiating ssa-form programs. *CoRR*, abs/1810.07951, 2018.
- [7] Tim Besard, Christophe Foket, and Bjorn De Sutter. Effective extensible programming: Unleashing Julia on GPUs. *IEEE Transactions on Parallel and Distributed Systems*, 2018.
- [8] Tim Besard, Valentin Churavy, Alan Edelman, and Bjorn De Sutter. Rapid software prototyping for heterogeneous and distributed platforms. *Advances in Engineering Software*, 132:29–46, 2019.
- [9] Valentin Churavy. KernelAbstractions.jl.
- [10] Sibyll Schaphoff, Werner von Bloh, Anja Rammig, Kirsten Thonicke, Hester Biemans, Matthias Forkel, Dieter Gerten, Jens Heinke, Jonas Jägermeyr, Jürgen Knauer, et al. Lpjml4—a dynamic global vegetation model with managed land—part 1: Model description. *Geoscientific Model Development*, 11(4):1343–1375, 2018.
- [11] Graham D Farquhar, S von von Caemmerer, and Joseph A Berry. A biochemical model of photosynthetic co2 assimilation in leaves of c3 species. *planta*, 149(1):78–90, 1980.
- [12] Graham D Farquhar and S Von Caemmerer. Modelling of photosynthetic response to environmental conditions. In *Physiological plant ecology II: Water relations and carbon assimilation*, pages 549–587. Springer, 1982.

- [13] G James Collatz, J Timothy Ball, Cyril Grivet, and Joseph A Berry. Physiological and environmental regulation of stomatal conductance, photosynthesis and transpiration: a model that includes a laminar boundary layer. *Agricultural and Forest meteorology*, 54(2-4):107–136, 1991.
- [14] G James Collatz, Miquel Ribas-Carbo, and Joseph A Berry. Coupled photosynthesis-stomatal conductance model for leaves of c4 plants. *Functional Plant Biology*, 19(5):519–538, 1992.
- [15] Alex Haxeltine and IC Prentice. A general model for the light-use efficiency of primary production. *Functional Ecology*, pages 551–561, 1996.
- [16] I Colin Prentice, Martin Heimann, and Stephen Sitch. The carbon balance of the terrestrial biosphere: Ecosystem models and atmospheric observations. *Ecological Applications*, 10(6):1553–1573, 2000.
- [17] Yiqi Luo, Yuanyuan Huang, Carlos A Sierra, Jianyang Xia, Anders Ahlström, Yizhao Chen, Oleksandra Hararuk, Enqing Hou, Lifen Jiang, Cuijuan Liao, et al. Matrix approach to land carbon cycle modeling. *Journal of Advances in Modeling Earth Systems*, 14(7):e2022MS003008, 2022.
- [18] Stephen Sitch, Benjamin Smith, I Colin Prentice, Almut Arneth, Alberte Bondeau, Wolfgang Cramer, Jed O Kaplan, Samuel Levis, Wolfgang Lucht, M Thonicke Sykes, et al. Evaluation of ecosystem dynamics, plant geography and terrestrial carbon cycling in the lpj dynamic global vegetation model. *Global change biology*, 9(2):161–185, 2003.
- [19] Werner von Bloh, Sibyll Schaphoff, Christoph Müller, Susanne Rolinski, Katharina Waha, and Sönke Zaehle. Implementing the nitrogen cycle into the dynamic global vegetation, hydrology, and crop growth model lpjml (version 5.0). *Geoscientific Model Development*, 11(7):2789–2812, 2018.
- [20] Stefanie Rost, Dieter Gerten, Alberte Bondeau, Wolfgang Lucht, Janine Rohwer, and Sibyll Schaphoff. Agricultural green and blue water consumption and its influence on the global water system. *Water Resources Research*, 44(9), 2008.
- [21] Sara Minoli, Jonas Jägermeyr, Senthold Asseng, Anton Urfels, and Christoph Müller. Global crop yields can be lifted by timely adaptation of growing periods to climate change. *Nature Communications*, 13(1):7079, 2022.
- [22] Markus Reichstein, Eva Falge, Dennis Baldocchi, Dario Papale, Marc Aubinet, Paul Berbigier, Christian Bernhofer, Nina Buchmann, Tagir Gilmanov, Andre Granier, et al. On the separation of net ecosystem exchange into assimilation and ecosystem respiration: review and improved algorithm. *Global change biology*, 11(9):1424–1439, 2005.

- [23] Gilberto Pastorello, Carlo Trotta, Eleonora Canfora, Housen Chu, Danielle Christianson, You-Wei Cheah, Cristina Poindexter, Jiquan Chen, Abdelrahman Elbashandy, Marty Humphrey, et al. The fluxnet2015 dataset and the oneflux processing pipeline for eddy covariance data. *Scientific data*, 7(1):225, 2020.
- [24] Ilya Loshchilov and Frank Hutter. Decoupled weight decay regularization. *arXiv preprint arXiv:1711.05101*, 2017.
- [25] Nina Buchmann, Lukas Hortnagl, Sabina Keller, and Fabio Turco. Fluxnet Product from Oensingen crop, 2003–2023. <https://hdl.handle.net/11676/IWly2Cb3xiVw8QB-Z1SXWqKx>, 2024. Accessed 2025-07-30.
- [26] Youngryel Ryu, Minseok Kang, and Jongho Kim. FLUXNET-CH4 KR-CRK Cheorwon Rice paddy, Dataset. <https://doi.org/10.18140/FLX/1669649>, 2020. Data collected from 2015–2018. Accessed 2025-07-30.
- [27] Adam Schreiner-McGraw. AmeriFlux FLUXNET-1F US-Mo3 LTAR CMRB Field 3 (CMRB BAU), Ver. 3-5, AmeriFlux AMP, Dataset. <https://doi.org/10.17190/AMF/2229384>, 2023. Accessed 2025-07-30.
- [28] Andy Suyker. AmeriFlux FLUXNET-1F US-Ne1 Mead - irrigated continuous maize site, Ver. 4-7, AmeriFlux AMP, (Dataset). <https://doi.org/10.17190/AMF/1871140>, 2025. Accessed 2025-07-30.
- [29] Giulia Ronchetti, Luigi Nisini Scacchiafichi, Lorenzo Seguini, Iacopo Cerrani, and Marijn van der Velde. Harmonized european union subnational crop statistics can reveal climate impacts and crop cultivation shifts. *Earth System Science Data*, 16(3):1623–1649, 2024.
- [30] Fluxnet Product from Lonzeo crop, 2004–2020. [https://hdl.handle.net/11676/eo.cBxOeMONH2G8z4g0G\\_60J](https://hdl.handle.net/11676/eo.cBxOeMONH2G8z4g0G_60J), 2021. Accessed 2025-07-30.
- [31] Fluxnet Product from Gebesee crop, 2001–2020. <https://hdl.handle.net/11676/ICpbHZew62rMezJ0DdGd1QZz>, 2021. Accessed 2025-07-30.
- [32] Fluxnet Product from Klingenberg crop, 2004–2023. <https://hdl.handle.net/11676/b8wQzTvW2nkN-mFPaSIO6lad>, 2021. Accessed 2025-07-30.
- [33] Fluxnet Product from Selhausen Juelich crop, 2011–2014. [https://hdl.handle.net/11676/HE7Nj8\\_yV0xTr1zYLVochSR1](https://hdl.handle.net/11676/HE7Nj8_yV0xTr1zYLVochSR1), 2021. Accessed 2025-07-30.
- [34] Marius Schmidt Karl Schneider. FLUXNET2015 DE-Seh Selhausen, Dataset. <https://doi.org/10.18140/FLX/1669649>, 2020. Data collected from 2015–2018. Accessed 2025-07-30.
- [35] Fluxnet Product from Voulundgaard crop, 2009–2018. <https://hdl.handle.net/11676/Msw4MfzUvAI4JRy4PEXnxRdg>, 2024. Accessed 2025-07-30.

- [36] Pauline Buysse, Brigitte Durand, Jean-Christophe Gueudet, Nicolas Mascher, Eric Larmanou, Pierre Cellier, and Benjamin Loubet. FLUXNET2015 FR-Gri Grignon, Dataset. <https://doi.org/10.18140/FLX/1669649>, 2020. Data collected from 2004-2014. Accessed 2025-07-30.
- [37] Fluxnet Product from Aurade crop, 2005-2023. <https://hdl.handle.net/11676/8VEnzKK7Clppzc7jrXIMFAIc>, 2021. Accessed 2025-07-30.
- [38] Fluxnet Product from Estrees-Mons A28 crop, 2017-2023. [https://hdl.handle.net/11676/iFrHZC8K\\_-lgFIKzoAQOXoc9](https://hdl.handle.net/11676/iFrHZC8K_-lgFIKzoAQOXoc9), 2021. Accessed 2025-07-30.
- [39] Fluxnet Product from Lamasquere crop, 2005-2020. <https://hdl.handle.net/11676/7WGNecqpODsIXmZfRvQxboSm>, 2021. Accessed 2025-07-30.
- [40] Simone Sabbatini, Nicola Arriga, Beniamino Gioli, Dario Papale, Michele Tomassucci, and Alessio Boschi. FLUXNET2015 IT-CA2 Castel d’Asso2, Dataset. <https://doi.org/10.18140/FLX/1440231>, 2020. Data collected from 2011-2014. Accessed 2025-07-30.
- [41] Jillian M Deines, Sotirios V Archontoulis, Isaiah Huber, and David B Lobell. Observational evidence for groundwater influence on crop yields in the united states. *Proceedings of the National Academy of Sciences*, 121(36):e2400085121, 2024.
- [42] Camilo Rey-Sanchez, Carlos Tianxin Wang, Daphne Szutu, Kyle Hemes, Joseph Verfaillie, and Dennis Baldocchi. AmeriFlux FLUXNET-1F US-Bi2 Bouldin Island corn, Ver. 3-5, AmeriFlux AMP, (Dataset). <https://doi.org/10.17190/AMF/1871135>, 2022. Accessed 2025-07-30.
- [43] Adam Schreiner-McGraw. AmeriFlux FLUXNET-1F US-Mo1 LTAR CMRB Field 1 (CMRB ASP), Ver. 5-7, AmeriFlux AMP, (Dataset). <https://doi.org/10.17190/AMF/2229382>, 2025. Accessed 2025-07-30.
- [44] Adam Schreiner-McGraw. AmeriFlux FLUXNET-1F US-Mo3 LTAR CMRB Field 3 (CMRB BAU), Ver. 3-5, AmeriFlux AMP, (Dataset). <https://doi.org/10.17190/AMF/2229384>, 2023. Accessed 2025-07-30.
- [45] Andy Suyker. AmeriFlux FLUXNET-1F US-Ne2 Mead - irrigated maize-soybean rotation site, Ver. 3-7, AmeriFlux AMP, (Dataset). <https://doi.org/10.17190/AMF/2574638>, 2025. Accessed 2025-07-30.
- [46] Andy Suyker. AmeriFlux BASE US-Ne3 Mead - rainfed maize-soybean rotation site, Ver. 19-5, AmeriFlux AMP, (Dataset). <https://doi.org/10.17190/AMF/1246086>, 2025. Accessed 2025-07-30.
- [47] John Baker and Tim Griffis. AmeriFlux FLUXNET-1F US-Ro1 Rosemount- G21, Ver. 5-7, AmeriFlux AMP, (Dataset). <https://doi.org/10.17190/AMF/1881588>,

2025. Accessed 2025-07-30.
- [48] John Baker and Tim Griffis. AmeriFlux FLUXNET-1F US-Ro3 Rosemount- G19, Ver. 4-7, AmeriFlux AMP, (Dataset). <https://doi.org/10.17190/AMF/2469468>, 2025. Accessed 2025-07-30.
- [49] John Baker and Tim Griffis. AmeriFlux FLUXNET-1F US-Ro5 Rosemount I18\_South, Ver. 5-7, AmeriFlux AMP, (Dataset). <https://doi.org/10.17190/AMF/1818371>, 2025. Accessed 2025-07-30.
- [50] John Baker and Tim Griffis. AmeriFlux FLUXNET-1F US-Ro6 Rosemount I18\_North, Ver. 5-7, AmeriFlux AMP, (Dataset). <https://doi.org/10.17190/AMF/1881590>, 2025. Accessed 2025-07-30.
- [51] Sergio M Vicente-Serrano, Santiago Beguería, and Juan I López-Moreno. A multiscalar drought index sensitive to global warming: the standardized precipitation evapotranspiration index. *Journal of climate*, 23(7):1696–1718, 2010.